

# Supplementary information

## Distinguishing Biotic and Abiotic Iron Oxidation at Low Temperatures

*Brian St Clair<sup>1,2,\*†</sup>, Justin Pottenger<sup>1</sup>, Randall Debes<sup>1,4</sup>, Kurt Hanselmann<sup>3</sup>, Everett Shock<sup>1,4,5</sup>*

1. Group Exploring Organic Processes in Geochemistry, Arizona State University, Tempe, AZ 85287, USA

2. Environmental Life Sciences, Arizona State University, Tempe, AZ 85287, USA

3. Swiss Federal Institute of Technology (ETH) Zurich, Department of Earth Sciences, Zürich, CH-8092, Switzerland

4. School of Earth & Space Exploration, Arizona State University, Tempe, AZ 85287, USA

5. School of Molecular Sciences, Arizona State University, Tempe, AZ 85287, USA

## Contents

#	section	page
S1	Estimated thermodynamic properties of aqueous metal carbonate and bicarbonate complexes	3
S2	Site descriptions and geographical information	14
S3	Field rate experiments	24
S4	Supplementary geochemical data	43
S5	Microbial community data	47
	References for Supplementary Material	53

## **S1 - Estimated thermodynamic properties of aqueous metal carbonate and bicarbonate complexes**

Speciation calculations for fluids in natural systems require equilibrium constants for the formation of chemical species over wide ranges of temperature and pressure. Over the last few decades several equilibrium constants for the formation of metal carbonate and bicarbonate complexes were measured at the reference conditions of 25°C and 1 bar. With additional thermodynamic properties, equilibrium constants for metal-ligand association reactions can be estimated at other temperatures and pressures. One approach is to use the revised-Helgeson-Kirkham-Flowers (HKF) equation of state<sup>50,69</sup> to calculate equilibrium constants at temperatures higher or lower than 25°C. A summary of the revised-HKF equation of state is found in Canovas and Shock<sup>70</sup>. As part of the present project, standard state thermodynamic properties of the species ( $\Delta\bar{G}_f^\circ, \Delta\bar{H}_f^\circ, \bar{S}^\circ, \bar{C}_p^\circ$ ) and revised-HKF equation-of-state parameters ( $c_1, c_2, \omega$ ) were calculated or estimated using established methods<sup>42,45,47,48,49,71</sup>. Here we summarize the methods used to generate the thermodynamic properties and revised-HKF parameters for aqueous metal carbonate and bicarbonate complexes. We start with a summary of the available standard state equilibrium constants and corresponding standard Gibbs energy of association reactions. The standard states adopted here are unit fugacity of pure gases at any temperature and 1 bar, unit activity for pure minerals and pure liquids at any temperature and pressure, and unit activity of hypothetical one molal aqueous solutes referenced to infinite dilution at any temperature and pressure.

### **S1.2 Standard Gibbs Energy of Formation ( $\Delta\bar{G}_f^\circ$ )**

Standard Gibbs energies of formation for each aqueous complex can be obtained from equilibrium constants for association reactions, together with the standard Gibbs energies of formation of the aqueous ions that form the complex. Equilibrium association constants for aqueous metal carbonate and bicarbonate species selected in this study are listed in Table S1, where it can be seen that in some cases equilibrium constant data were scrutinized in reviews. Experimental equilibrium data for some species are limited. In cases with multiple data sets we have attempted to choose the most reliable experimental data based on experimental procedures and associated uncertainties. Given the data in Table S1, there are two challenges

to geochemical modeling. One is to estimate missing values, especially for the abundant cations that can be present in natural waters ( $\text{Na}^+$ ,  $\text{K}^+$ ,  $\text{NH}_4^+$ , etc.). The other is to extrapolate the available data from the reference conditions to temperatures and pressures that prevail in natural systems.

Recent critical reviews recommend equilibrium constants for  $\text{Fe}^{2+}$ ,  $\text{Cu}^{2+}$ ,  $\text{Cd}^{2+}$ ,  $\text{Zn}^{2+}$  and  $\text{Pb}^{2+}$  bicarbonate and first and second carbonate complexes at the reference conditions, as well as  $\text{FeSO}_4$  (aq), as listed in Table S1. Earlier efforts to estimate revised-HKF parameters for complexes included bicarbonate and carbonate complexes of  $\text{Ag}^+$ ,  $\text{Ca}^{2+}$ ,  $\text{Mg}^{2+}$ ,  $\text{Sr}^{2+}$ ,  $\text{Ba}^{2+}$ , trivalent rare earth cations, and  $\text{Am}^{3+}$ <sup>45,48,49,72</sup>, and the strategy outlined below maintains quantitative consistency with those efforts. With the exceptions of  $\text{Na}^+$  and  $\text{Ag}^+$ , equilibrium constants for most monovalent cation carbonate complexes have not been determined from experiments. While they are likely to be only feebly associated in conditions common in natural systems on Earth's surface, the potentially high abundance of some monovalent cations means they should not be neglected in speciation calculations. Correlations permit estimation of  $\Delta_r \bar{G}^\circ$  for these complex association reactions<sup>48,71</sup>. An example is shown in Fig S1 involving standard Gibbs energies of reactions to form oxalate, formate, carbonate and bicarbonate complexes. The error bars shown in this figure do not represent experimental uncertainty, but instead indicate a  $\pm 0.5$  log unit range in the association constant that is the target for estimates of greatest use in geochemical modeling<sup>45</sup>. The correlation in Fig S1 is given by

$$\Delta_r \bar{G}^\circ(\text{carbonate or bicarbonate}) = 1.183 \Delta_r \bar{G}^\circ(\text{oxalate or formate}) + 740. \quad (\text{A1}),$$

which allows estimates of data missing from experiments. In this study, we applied this correlation to estimate standard Gibbs energies of association for  $\text{K}(\text{CO}_3)^-$  and  $\text{NH}_4(\text{CO}_3)^-$  from data for oxalate complexes from Prapaipong et al.<sup>71</sup>. Additionally, values of  $\Delta_r \bar{G}^\circ$  for  $\text{Li}(\text{CO}_3)^-$  and  $\text{Rb}(\text{CO}_3)^-$  were estimated using Eqn. A1 from values for oxalate complexes estimated by Prapaipong et al.<sup>71</sup>, and  $\text{K}(\text{HCO}_3)$  (aq) from data for formate complexes estimated by Shock and Koretsky<sup>48</sup>. These estimates have inherently higher uncertainty and values should be considered provisional. Experiments will ultimately reveal the accuracy of these estimations. The resulting standard Gibbs energies of formation of the complexes are listed in table S2, together with other standard state data and equation of state parameters estimated as described below.

Table S1 – Selected equilibrium association constants for carbonate, bicarbonate, and sulfate aqueous complexes.

Cation	Complex	Log K*	Data Source	Data Critique%
Fe <sup>2+</sup>	Fe(CO <sub>3</sub> )	5.45	25	27, 28
	Fe(HCO <sub>3</sub> ) <sup>+</sup>	1.47	25	27, 28
	Fe(CO <sub>3</sub> ) <sub>2</sub> <sup>-2</sup>	7.1	73	27, 28
	Fe(SO <sub>4</sub> )	2.44	74	28
Cu <sup>2+</sup>	Cu(HCO <sub>3</sub> ) <sup>+</sup>	1.84	75	93
	Cu(CO <sub>3</sub> )	6.75	76	93
	Cu(CO <sub>3</sub> ) <sub>2</sub> <sup>-2</sup>	10.3	76	93
Cd <sup>2+</sup>	Cd(CO <sub>3</sub> )	4.4	77	94
	Cd(HCO <sub>3</sub> ) <sup>+</sup>	2	78	94
Zn <sup>2+</sup>	Zn(CO <sub>3</sub> )	4.75	79	95
	Zn(CO <sub>3</sub> ) <sub>2</sub> <sup>-2</sup>	5.4	80	95
	Zn(HCO <sub>3</sub> ) <sup>+</sup>	1.62	81	95
Pb <sup>2+</sup>	Pb(CO <sub>3</sub> )	6.45	82	96
	Pb(CO <sub>3</sub> ) <sub>2</sub> <sup>-2</sup>	10.13	82	96
	Pb(HCO <sub>3</sub> ) <sup>+</sup>	2.39	83	96
Co <sup>2+</sup>	Co(CO <sub>3</sub> )	4.41	79	-
	Co(HCO <sub>3</sub> ) <sup>+</sup>	2.2	79	-
Ni <sup>2+</sup>	Ni(CO <sub>3</sub> )	4.83	79	-
	Ni(HCO <sub>3</sub> ) <sup>+</sup>	2.22	79	-
Mn <sup>2+</sup>	Mn(CO <sub>3</sub> )	4.7	84	-
	Mn(HCO <sub>3</sub> ) <sup>+</sup>	1.96	85	-
Na <sup>+</sup>	Na(CO <sub>3</sub> ) <sup>-</sup>	0.575	86	-
	Na(HCO <sub>3</sub> )	0.161	86	-
K <sup>+</sup>	K(HCO <sub>3</sub> )	-0.26 <sup>&amp;</sup>	87	
Ag <sup>+</sup>	Ag(CO <sub>3</sub> ) <sup>-</sup>	2.69	88	45
	Ag(CO <sub>3</sub> ) <sub>2</sub> <sup>-3</sup>	2.15	88	45
Mg <sup>2+</sup>	Mg(HCO <sub>3</sub> ) <sup>+</sup>	1.04	89	48 <sup>^</sup>
	Mg(CO <sub>3</sub> )	2.98	89	45
Ca <sup>2+</sup>	Ca(HCO <sub>3</sub> ) <sup>+</sup>	1.05	90	48 <sup>^</sup>
	Ca(CO <sub>3</sub> )	3.33	90	45
Sr <sup>2+</sup>	Sr(HCO <sub>3</sub> ) <sup>+</sup>	1.23	91	48 <sup>^</sup>
	Sr(CO <sub>3</sub> )	2.87	91	45
Ba <sup>2+</sup>	Ba(HCO <sub>3</sub> ) <sup>+</sup>	1.02	92	48 <sup>^</sup>
	Ba(CO <sub>3</sub> )	2.65	92	45

\*log K refers to the association reaction to form the complex from the ions at 25°C, 1 bar, and ionic strength of 0.<sup>&</sup>Log K at 38°C; The value adopted for this study was estimated with Eqn. A1. <sup>^</sup>Equilibrium constants used by Shock & Koretsky<sup>45</sup> were not reported by those authors, but correspond to the values listed. <sup>%</sup>Data Critique refers to a critical review of available equilibrium constants that were used to select the value listed in the table. Selections of additional values were based on an evaluation in this study of the most reliable data, or, in some cases, inclusion of the only available data.

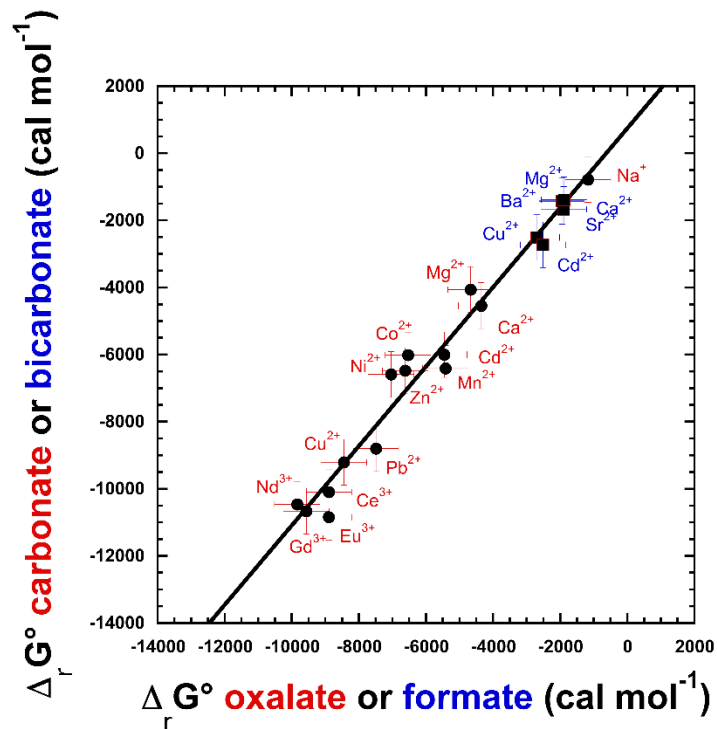


**Figure S1** - Correlation of standard Gibbs energies of association for various aqueous complexes. Data for carbonate and bicarbonate complexes from Table S1 and Haas et al.<sup>72</sup>, for oxalate complexes from Prapaipong et al.<sup>71</sup> and for formate complexes from Shock & Koretsky<sup>48</sup>. Error bars do not represent experimental uncertainty but instead signify  $\pm 0.5$  log unit windows around each association constant, which renders an estimation method useful. The correlation shown was obtained by least squares regression and has  $R^2 = 0.98$  and is given by Eqn (A1)

Table S2 - Summary of standard partial molal thermodynamic data at 25°C and 1 bar for aqueous metal carbonate and bicarbonate species, along with charge (Z) and revised-HKF equation of state parameters required to calculate the corresponding properties at elevated temperatures.

Species	$\Delta G_f^{\circ a}$	$\Delta H_f^{\circ a}$	$S^{\circ b}$	$C_p^{\circ b}$	$c1^b$	$c2^c \times 10^{-4}$	$\omega^a \times 10^{-5}$	Z
FeCO <sub>3</sub>	-155442	-183875	-13.97	-30.00	-11.7653	-9.1456	-0.0380	0
MnCO <sub>3</sub>	-187703	-213178	-2.93	-26.20	-9.5383	-8.3715	-0.0380	0
ZnCO <sub>3</sub>	-167872	-197642	-15.06	-27.43	-10.2592	-8.6221	-0.0380	0
CuCO <sub>3</sub>	-119725	-147820	-11.42	-27.80	-10.4760	-8.6975	-0.0380	0
CdCO <sub>3</sub>	-150754	-178085	-4.39	-25.60	-9.1867	-8.2493	-0.0380	0
PbCO <sub>3</sub>	-140701	-161150	21.81	-34.80	-14.5784	-10.1234	-0.0380	0
CoCO <sub>3</sub>	-145208	-174468	-16.03	-29.90	-11.7067	-9.1252	-0.0380	0
NiCO <sub>3</sub>	-143681	-174283	-20.64	-33.80	-13.9924	-9.9197	-0.0380	0
Fe(CO <sub>3</sub> ) <sub>2</sub> <sup>-2</sup>	-283939	-354507	-33.02	-56.10	7.4869	-14.4622	3.7120	-2
Zn(CO <sub>3</sub> ) <sub>2</sub> <sup>-2</sup>	-294950	-366798	-34.11	-53.53	9.1454	-13.9387	3.7286	-2
Cu(CO <sub>3</sub> ) <sub>2</sub> <sup>-2</sup>	-250760	-321123	-30.47	-53.90	8.4209	-14.0140	3.6735	-2
Pb(CO <sub>3</sub> ) <sub>2</sub> <sup>-2</sup>	-271913	-336371	2.76	-60.90	-0.3186	-15.4399	3.1701	-2
NaCO <sub>3</sub> <sup>-</sup>	-189567	-223464	-10.94	-8.82	-12.4895	-4.8318	-1.4638	-1
KCO <sub>3</sub> <sup>-</sup>	-194252	-215525	17.89	-16.12	-20.7896	-6.3182	-1.9005	-1
LiCO <sub>3</sub> <sup>-</sup>	-196650	-238469	-42.81	-3.90	-5.1587	-3.8290	-0.9812	-1
RbCO <sub>3</sub> <sup>-</sup>	-194535	-218275	31.05	-21.10	-25.5442	-7.3327	-2.0998	-1
NH <sub>4</sub> CO <sub>3</sub> <sup>-</sup>	-145926	-190926	24.74	-2.36	-13.6810	-3.5153	-2.0042	-1
Fe(HCO <sub>3</sub> ) <sup>+</sup>	-164158	-184997	11.50	55.02	41.8870	8.1736	0.3770	1
Mn(HCO <sub>3</sub> ) <sup>+</sup>	-198070	-214597	23.97	63.57	45.1584	9.9153	0.1882	1
Zn(HCO <sub>3</sub> ) <sup>+</sup>	-177692	-199910	10.27	60.81	45.4479	9.3515	0.3957	1
Cu(HCO <sub>3</sub> ) <sup>+</sup>	-127117	-147520	14.38	59.97	44.3866	9.1819	0.3334	1
Cd(HCO <sub>3</sub> ) <sup>+</sup>	-161571	-180938	22.33	64.92	46.1790	10.1903	0.2131	1
Pb(HCO <sub>3</sub> ) <sup>+</sup>	-149253	-160727	51.92	44.22	29.9188	5.9737	-0.2350	1
Co(HCO <sub>3</sub> ) <sup>+</sup>	-156284	-178030	9.17	55.25	42.3438	8.2195	0.4123	1
Ni(HCO <sub>3</sub> ) <sup>+</sup>	-154211	-176473	7.33	46.47	37.4577	6.4320	0.4401	1
Na(HCO <sub>3</sub> ) <sub>aq</sub>	-203093	-222193	38.69	47.88	33.9093	6.7192	-0.0347	0
K(HCO <sub>3</sub> ) <sub>aq</sub>	-207103	-219419	51.92	31.95	22.7051	3.4743	-0.2375	0
FeSO <sub>4</sub>	-203129	-238307	-5.8	-28.40	-10.8255	-8.8190	-0.0380	0

a. cal mol<sup>-1</sup>

b. cal mol<sup>-1</sup> K<sup>-1</sup>

c. cal K mol<sup>-1</sup>

### S1.3 $\Delta_r \bar{S}^\circ$ and $\Delta_r \bar{C}_p$

Methods for estimating standard partial molal entropies and heat capacities of aqueous carbonate complexes at the reference conditions exist but are incompletely documented. Sverjensky et al.<sup>45</sup> obtained standard partial molal entropy values at 25°C and 1 bar for several aqueous carbonate complexes through regression of experimental equilibrium dissociation constants available over various temperature ranges. They also provided correlations of standard partial molal entropies of association ( $\Delta_r \bar{S}^\circ$ ) with the standard partial molal entropies ( $\bar{S}^\circ$ ) of monovalent and divalent cations. Expressions for these correlations (resulting estimates are in calories) are given by

$$\Delta_r \bar{S}^\circ = 1.83 \bar{S}^\circ - 38.5 \quad (\text{A2})$$

for monovalent and

$$\Delta_r \bar{S}^\circ = 0.213 \bar{S}^\circ + 28.67 \quad (\text{A3})$$

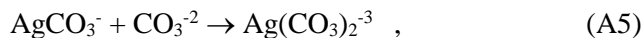
for divalent cations, which were used in the present study. Murphy and Shock<sup>49</sup> estimated  $\bar{S}^\circ$  for the carbonate complex of  $\text{Am}^{+3}$  and refer to methods provided by Sverjensky et al.<sup>45</sup>, who offer no correlation for trivalent cations. What Murphy and Shock<sup>49</sup> did was construct a provisional correlation for trivalent cations based on the slopes and intercepts of the monovalent and divalent correlations from Sverjensky et al.<sup>45</sup> given by Eqns. (A2) and (A3), inspired by the existence of correlations for sulfate complexes for all three cation charges, and the observation by Sverjensky et al.<sup>45</sup> that correlations of slope with cation charge as well as intercept with cation charge exist for the three sulfate-complex correlations. The resulting predicted correlation for trivalent-cation complexes of carbonate is

$$\Delta_r \bar{S}^\circ = -1.4 \bar{S}^\circ + 95.8 \quad (\text{A4})$$

Murphy and Shock<sup>49</sup> also made an estimate of  $\bar{S}^\circ$  of the second carbonate complex of  $\text{Am}^{+3}$ , leaving only the cryptic message in a footnote that the value was “estimated with methods developed in this study based on those described by Sverjensky et al. (1997)...” without elaborating further. Sverjensky et al.<sup>45</sup> obtained reference state values of  $\bar{S}^\circ$  of the first (0 cal mol<sup>-1</sup> K<sup>-1</sup>) and second (-19 cal mol<sup>-1</sup> K<sup>-1</sup>) carbonate



complexes of  $\text{Ag}^+$  by regression of equilibrium constant data. These values can be combined with  $\bar{S}^\circ$  of the carbonate ion ( $-11.95 \text{ cal mol}^{-1} \text{ K}^{-1}$ )<sup>43</sup> to calculate the standard entropy of the reaction



giving  $-7.1 \text{ cal mol}^{-1} \text{ K}^{-1}$ . Murphy and Shock<sup>49</sup> used this value and their data for  $\text{Am}^{+3}$  and  $\text{AmCO}_3^+$  to estimate  $\bar{S}^\circ$  of  $\text{Am}(\text{CO}_3)_2^-$ . This strategy was adopted in the present study to estimate reference state values of  $\bar{S}^\circ$  for second carbonate complexes. In contrast, the standard partial molar entropy for  $\text{FeSO}_4(\text{aq})$  is calculated from the  $\Delta_r \bar{S}^\circ$  documented by Smith and Martell<sup>97</sup>.

Regression of accurate standard partial molal heat capacity ( $\bar{C}_P^\circ$ ) values at the reference conditions for aqueous complexes from equilibrium dissociation constants requires data at temperatures  $> 100^\circ\text{C}$ . Sverjensky et al.<sup>45</sup> found that experimentally determined equilibrium constants in this temperature range for inorganic complexes involving divalent ligands were extremely rare, and obtained  $\bar{C}_P^\circ$  values for only two sulfate complexes,  $\text{KSO}_4^+$  and  $\text{CaSO}_4^\circ$ , via regression. They used these values to calculate standard partial molal heat capacities of association ( $\Delta_r \bar{C}_P^\circ$ ) for the two complexes from

$$\Delta_r \bar{C}_P^\circ = \bar{C}_{P,\text{complex}}^\circ - \bar{C}_{P,\text{cation}}^\circ - \bar{C}_{P,\text{ligand}}^\circ \quad (\text{A6})$$

and used the resulting  $\Delta_r \bar{C}_P^\circ$  values for sulfate complexes of monovalent ( $51.4 \text{ cal mol}^{-1} \text{ K}^{-1}$ ) and divalent ( $47.4 \text{ cal mol}^{-1} \text{ K}^{-1}$ ) cations to make estimates. On the one hand they estimated  $\bar{C}_P^\circ$  for  $\text{MnSO}_4^\circ$  and used the estimate together with experimental dissociation constants to obtain a value of  $\bar{S}^\circ$  for this complex. On the other, they also used these values of  $\Delta_r \bar{C}_P^\circ$  to estimate values of  $\bar{C}_P^\circ$  for *carbonate* complexes, citing the relatively small difference in the values of  $\bar{C}_P^\circ$  for sulfate ( $-64.38 \text{ cal mol}^{-1} \text{ K}^{-1}$ ) and carbonate ( $-69.5 \text{ cal mol}^{-1} \text{ K}^{-1}$ ) as justification for this estimation strategy, and cautioning that equilibrium constants obtained above  $100^\circ\text{C}$  using this strategy should be considered “provisional estimates”. Because we adopted this same estimation strategy for carbonate complexes, that same caution should be applied to using the results of the present study at temperatures  $> 100^\circ\text{C}$ .

Murphy and Shock<sup>49</sup> extended this estimation strategy to divalent-ligand complexes of trivalent cations with a cryptic footnote about “methods deduced from Sverjensky et al. (1997)”. What they did was

take the difference between the two  $\Delta_r \bar{C}_P^\circ$  values calculated with Eqn (5) for monovalent and divalent cations (4 cal mol<sup>-1</sup> K<sup>-1</sup>) and estimated 43.4 cal mol<sup>-1</sup> K<sup>-1</sup> for  $\Delta_r \bar{C}_P^\circ$  for the association reaction forming sulfate complexes of trivalent cations, which they used to estimate  $\bar{C}_P^\circ$  for AmSO<sub>4</sub><sup>+</sup> and AmCO<sub>3</sub><sup>+</sup>. Their estimates of  $\bar{C}_P^\circ$  for the second sulfate and carbonate complexes were obtained by using the same value of  $\Delta_r \bar{C}_P^\circ$  a second time. In effect, using 43.4 cal mol<sup>-1</sup> K<sup>-1</sup> as  $\Delta_r \bar{C}_P^\circ$  in the relation

$$\Delta_r \bar{C}_P^\circ = \bar{C}_{P,2nd\ complex}^\circ - \bar{C}_{P,1st\ complex}^\circ - \bar{C}_{P,ligand}^\circ \quad , \quad (A7)$$

and solving for  $\bar{C}_{P,2nd\ complex}^\circ$ . In the case of Am<sup>+3</sup> complexes this yields -77.8 cal mol<sup>-1</sup> K<sup>-1</sup> for Am(SO<sub>4</sub>)<sub>2</sub><sup>-</sup> and -88.0 cal mol<sup>-1</sup> K<sup>-1</sup> for Am(CO<sub>3</sub>)<sub>2</sub><sup>-</sup>. The latter value is opposite in sign to the value reported by Murphy and Shock<sup>49</sup>, which we have determined is a typographical error. The justification for Eqn (A7) is unclear, although it should be noted that Sverjensky et al.<sup>45</sup> used the same approach to estimate  $\bar{C}_P^\circ$  for Ag(CO<sub>3</sub>)<sub>2</sub><sup>-3</sup>, using the monovalent cation value of 51.4 cal mol<sup>-1</sup> K<sup>-1</sup>, which was then used to regress low-temperature equilibrium constants to obtain  $\bar{S}^\circ$  for that complex. In this context, it is worth noting that in section 5 of Sverjensky et al.<sup>45</sup> there is a subsection 5.1 about monovalent ligands, but no corresponding subsection 5.2 that may have, in the original manuscript, explained some of these estimation strategies for divalent ligands, and offered a justification for using Eqn (A7) the way it was used. It is odd to have a stand-alone subsection 5.1 with no other subsections. In any event, in the present study we used the methods outlined above to estimate values of  $\bar{C}_P^\circ$  for second carbonate complexes, and repeat the caution from Sverjensky et al.<sup>45</sup> that resulting equilibrium constants calculated above 100°C should be considered provisional estimates.

Calculated values of standard state properties at the reference conditions, obtained as described above, are listed in Table S2, together with revised-HKF equation-of-state parameters ( $c_1$ ,  $c_2$ , and  $\omega$ ) estimated with methods from Shock & Helgeson<sup>47</sup>, Shock et al.<sup>43</sup>, and Svejensky et al.<sup>45</sup>. These data were used in the speciation calculations discussed in the text, and can be used to calculate equilibrium constants for reactions involving these carbonate and bicarbonate complexes over wide ranges of temperature encountered in natural systems. Examples are given in Tables S3-S6.

Table S3. Log K for the formation of divalent metal carbonate aqueous species from 0 – 350 °C. Log K is for the reaction  $M^{2+} + CO_3^{2-} \rightarrow M(CO_3)^0$

species	Log K (25°C)	0°C	50°C	100°C	150°C	200°C	250°C	300°C	350°C
Fe(CO <sub>3</sub> )	5.41	5.528	5.450	5.578	5.848	6.277	6.923	7.930	9.572
Mn(CO <sub>3</sub> )	4.7	4.672	4.792	5.071	5.461	5.986	6.712	7.786	9.495
Zn(CO <sub>3</sub> )	4.75	4.772	4.803	5.022	5.364	5.851	6.546	7.593	9.265
Cu(CO <sub>3</sub> )	6.75	6.936	6.655	6.622	6.760	7.076	7.625	8.546	10.103
Cd(CO <sub>3</sub> )	4.4	4.350	4.511	4.821	5.231	5.769	6.501	7.574	9.304
Pb(CO <sub>3</sub> )	6.45	6.492	6.478	6.642	6.929	7.357	7.988	8.966	10.634
Co(CO <sub>3</sub> )	4.41	4.400	4.484	4.732	5.094	5.595	6.302	7.360	9.037
Ni(CO <sub>3</sub> )	4.83	4.873	4.857	5.024	5.321	5.769	6.429	7.447	9.081

Table S4. Log K for the formation of divalent metal carbonate (second association) species from 0 – 350 °C. Log K is for the reaction  $M^{2+} + 2 CO_3^{2-} \rightarrow M(CO_3)_2^{-2}$

species	Log K (25°C)	0°C	50°C	100°C	150°C	200°C	250°C	300°C	350°C
Fe(CO <sub>3</sub> ) <sub>2</sub> <sup>-2</sup>	7.17	7.949	6.696	6.266	6.277	6.612	7.259	8.326	10.184
Zn(CO <sub>3</sub> ) <sub>2</sub> <sup>-2</sup>	5.4	6.034	5.053	4.826	4.992	5.447	6.190	7.334	9.259
Cu(CO <sub>3</sub> ) <sub>2</sub> <sup>-2</sup>	10.3	11.332	9.611	8.829	8.563	8.675	9.139	10.051	11.751
Pb(CO <sub>3</sub> ) <sub>2</sub> <sup>-2</sup>	10.13	10.718	9.813	9.625	9.819	10.303	11.082	12.266	14.131

Table S5. Log K for the formation of monovalent metal carbonate species from 0 – 350 °C. Log K is for the reaction  $M^+ + CO_3^{2-} \rightarrow M(CO_3)^-$ . Log K at 25 °C for NaCO<sub>3</sub><sup>-</sup> is experimental, but all others are estimated (see text).

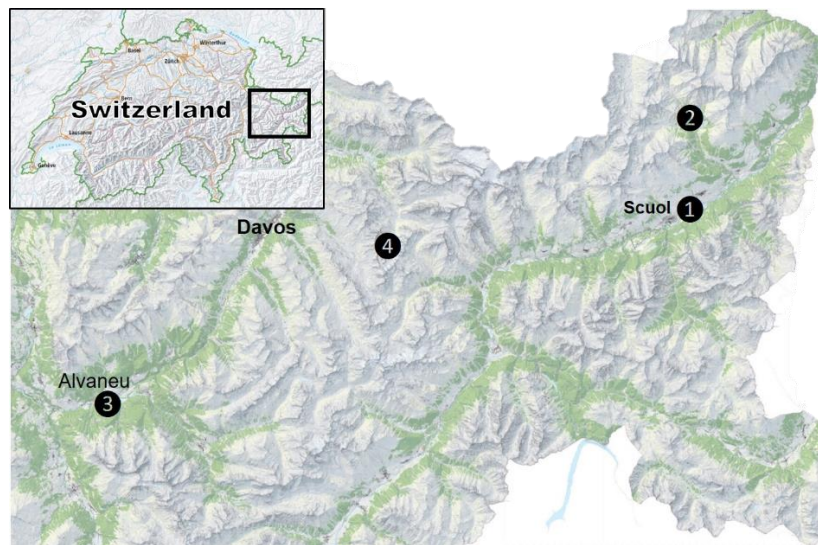
species	Log K 25 °C	0°C	50°C	100°C	150°C	200°C	250°C	300°C	350°C
Na(CO <sub>3</sub> ) <sup>-</sup>	0.575	0.94	0.344	0.118	0.136	0.405	1.032	2.36	6.014
K(CO <sub>3</sub> ) <sup>-</sup>	0.811	0.823	0.877	1.137	1.545	2.152	3.113	4.865	9.540
Li(CO <sub>3</sub> ) <sup>-</sup>	0.386	1.144	-0.179	-0.934	-1.319	-1.378	-1.058	-0.113	2.588
Rb(CO <sub>3</sub> ) <sup>-</sup>	0.399	0.203	0.640	1.179	1.799	2.578	3.699	5.652	10.82
NH <sub>4</sub> (CO <sub>3</sub> ) <sup>-</sup>	0.924	0.858	1.056	1.417	1.897	2.560	3.574	5.401	10.30

Table S6. Log K for the formation of divalent metal bicarbonate species from 0 – 350 °C. Log K is for the reaction  $M^{2+} + HCO_3^- \rightarrow MHCO_3^+$

species	Log K 25°C	0°C	50°C	100°C	150°C	200°C	250°C	300°C	350°C
Fe(HCO <sub>3</sub> ) <sup>+</sup>	1.47	1.411	1.626	2.063	2.593	3.196	3.893	4.746	5.876
Mn(HCO <sub>3</sub> ) <sup>+</sup>	1.96	1.894	2.147	2.632	3.212	3.869	4.622	5.542	6.748
Zn(HCO <sub>3</sub> ) <sup>+</sup>	2.2	2.219	2.296	2.642	3.104	3.655	4.308	5.125	6.220
Cu(HCO <sub>3</sub> ) <sup>+</sup>	1.84	1.799	1.980	2.387	2.888	3.466	4.139	4.973	6.076
Cd(HCO <sub>3</sub> ) <sup>+</sup>	2	1.936	2.168	2.638	3.207	3.850	4.588	5.487	6.696
Pb(HCO <sub>3</sub> ) <sup>+</sup>	2.39	2.191	2.656	3.253	3.896	4.588	5.367	6.323	7.679
Co(HCO <sub>3</sub> ) <sup>+</sup>	2.2	2.220	2.289	2.619	3.068	3.607	4.252	5.062	6.147
Ni(HCO <sub>3</sub> ) <sup>+</sup>	2.22	2.199	2.337	2.699	3.160	3.700	4.338	5.134	6.197

## S2 Site descriptions and geographical information

Samples were taken in September 2015 from springs and lakes in four areas in the southeastern area of the canton of Graubünden in the Swiss Alps: Rablönch, Val Sinestra, Alvaneu Bad, and the Jöri lakes (see Fig S2). Preliminary sampling was also performed on some locations in October 2012 (Table S7). The locations range in elevation from 920 to 2740 meters above sea level.



**Figure S2** – A map of northeastern Graubünden canton with sample areas indicated by numbers. 1 – Rablönch, 2 – Val Sinestra, 3 – Alvaneu Bad area. 4 - Jöri Lakes.. Sample information within each area can be found in Tables 1, 2, 4, and 6. GPS coordinates for each sample location are listed in Tables 1 and 2. Map used with the permission of the Swiss Federal Office of Topography, Swisstopo (JA100120).

## S2.1 Rablönch

The iron-carbonate spring Funtana Rablönch (official name) is situated on the North side of the Inn river in the Lower Engadin, 1.6 km east of the town of Scuol. It is located approximately 5 km east of the recently described iron-bicarbonate spring Fuschna<sup>5</sup>. The source water emerges into a concrete housing in an agricultural field. A map of the area showing spring features and sampling locations is given in Fig S3. The water has minimal contact with the atmosphere before it is piped 24 meters downhill, emerging in a storm drain under an access road. The main outflow produces a carbonate terrace composed mostly of calcite stretching approximately 60 meters down the hillside. Iron staining persists approximately 20 meters down the main outflow. The predominant flow was first sampled where it emerges on the downslope side of the road at ~25 L / min. A portion of the spring flow of water is diverted (~4 L / min) to a roadside spigot to allow residents to collect the mineral water. Iron mats, loosely structured sediments rich in iron oxidizing bacteria and ferric minerals, are produced near both outlets. Significant mineral precipitation frequently alters the flow path of the main channel in the carbonate terrace.

Complete geochemical sample suites (see methods below) were taken at three points along the main flow path indicated by the sample numbers in Fig S3. Profiles of pH, O<sub>2</sub>(aq), Fe(II), conductivity, and temperature along the main flow path are shown in Fig S3 (data in Table S18). The pH increases by almost two pH units over 20 meters, presumably due to CO<sub>2</sub> degassing. Dissolved oxygen increases steadily until it approaches atmospheric saturation at around 12 meters from the road outlet. Fe(II) steadily decreases from 100  $\mu$ m near the source to under 2  $\mu$ m at 20 meters. Conductivity fluctuates, but generally decreases from 1650  $\mu$ S as calcite precipitates. Additional field data from the Rablönch sample locations can be found in Table 1. Preliminary samples taken at the same locations in 2012 (Table S17) suggest that the chemical composition of the spring is stable. Oxidation rate experiments were performed in the main outflow iron mat, a downstream site with moderate iron staining, and a downstream location where Fe(II) is nearly depleted, as shown in Fig S3.

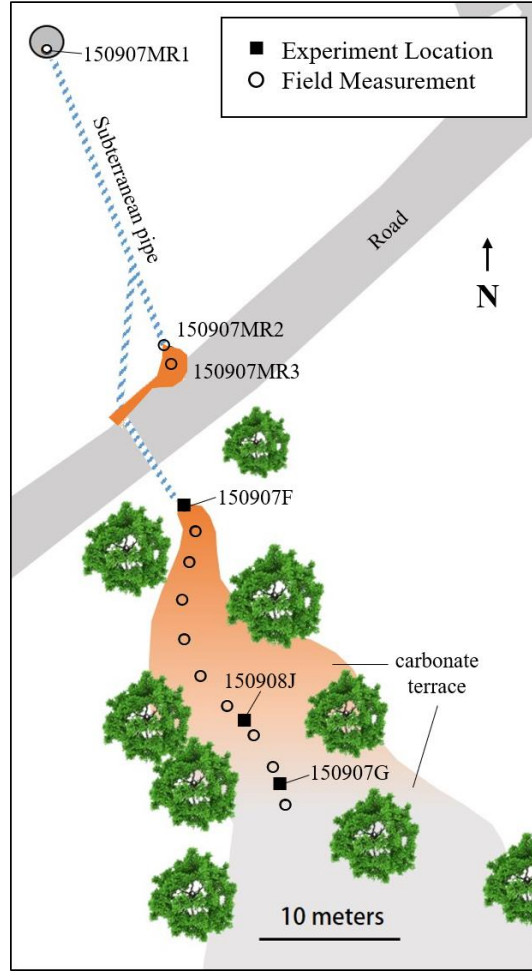


**Figure S3** – Map view sketch of Rablönch spring. Features are drawn to scale. The orange-fading-to-grey area indicates the carbonate terrace; the intensity of the orange indicates visible iron staining. The terrace continues off the diagram to the south for ~30 meters. The grey circle at top left shows a concrete housing for the spring source. Blue stippled lines show underground pipes, which at one point go under the road (grey strip). Green symbols are trees. Filled squares with sample IDs indicate locations where iron oxidation kinetics experiments were performed. Samples from these locations yielded field and lab geochemical datasets (see methods); open circles show locations of field measurements only. A profile of solutes in the outflow downstream of 150907F can be found in Fig S4.

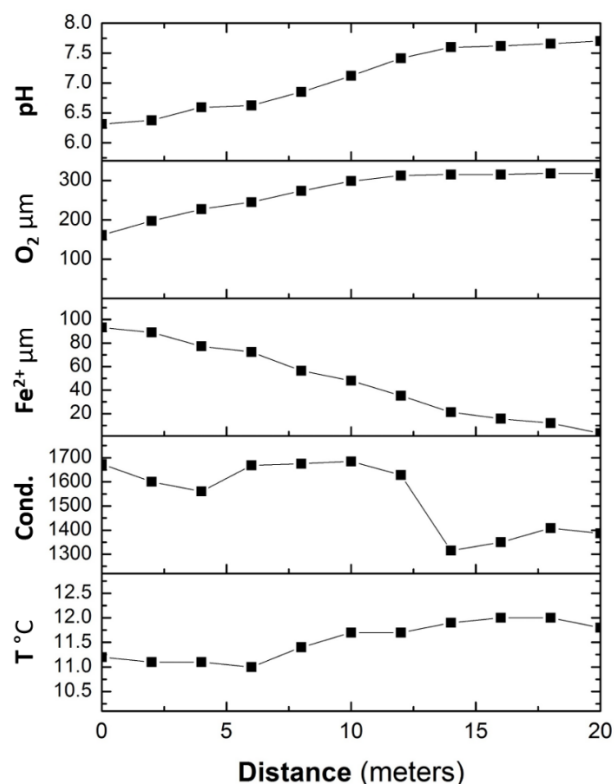


**Figure S4** – Profile of field data collected along the Rablönch spring outflow. Distance is measured from site 150907F and proceeds south along the main flow path depicted in Fig S3. The pH increases by > 1 pH unit down the outflow channel. Dissolved oxygen increases until it approaches saturation with air at around 12 meters. Ferrous iron is simultaneously depleted. The conductivity (in  $\mu\text{S}/\text{cm}$ ) follows a general downward trend but exhibits variability attributable to the diffuse flow path. The temperature changes less than  $1^\circ\text{C}$  throughout the outflow; which continues for  $\sim 10$  more meters down the terrace where the water becomes too shallow to make measurements.

## S2.2 Val Sinestra

The springs at Val Sinestra have high concentrations of iron and arsenic, and the water and sediment have been used historically as folk remedies to treat a wide variety of ailments. A grand hotel, clinic and bathhouse were built on the site, which was in use from the early 1800s until the closure of the hotel in the mid-1900s. Recent renovations for tourism have led to the site being reopened, though the springs are no longer a draw and remain inaccessible to the public. The source water of the springs is located in the now



dilapidated bathhouse. The springs have returned to a more natural appearing state with significant sediment accumulation, having been largely undisturbed for many decades. The volume of outgassing CO<sub>2</sub> is significant and can build up in the enclosed space, as evidenced by the numerous dead birds and mice in the decaying structure. Extreme caution should be used when sampling these springs to avoid the risk of asphyxiation. There are four spatially distinct sources of water that were also found to be compositionally different (see Table 1). Three of the springs precipitate a calcite layer on the water surface. The sediment in each spring is a deep orange color. Only one of the sources flows at a rate high enough to produce an outflow, as shown in the map of the area in Fig S5. This spring (sample number 150906C) is located under a trap door and flows 20 meters through an underground pipe to an outlet on the bank of La Brancla creek, a tributary of the Inn river. The outflow creates an orange iron-arsenic microbial mat that stretches for twelve meters before flowing into the creek. Samples were taken at each of the sources, as well as in the outflow. The field data profile for this outflow can be seen in Fig S6 (data in Table S19); note the break in scale between the source and the next sample more than 20 m downstream beyond the pipe. As at Rablönch, the pH increases down the outflow, although the increase is considerably smaller. O<sub>2</sub> increases down the outflow but never reaches saturation. The Fe(II) concentration is greater at Val Sinestra than at Rablönch, and its gentle decrease down the outflow is consistent with the slower abiotic oxidation rate in the lower pH outflow.

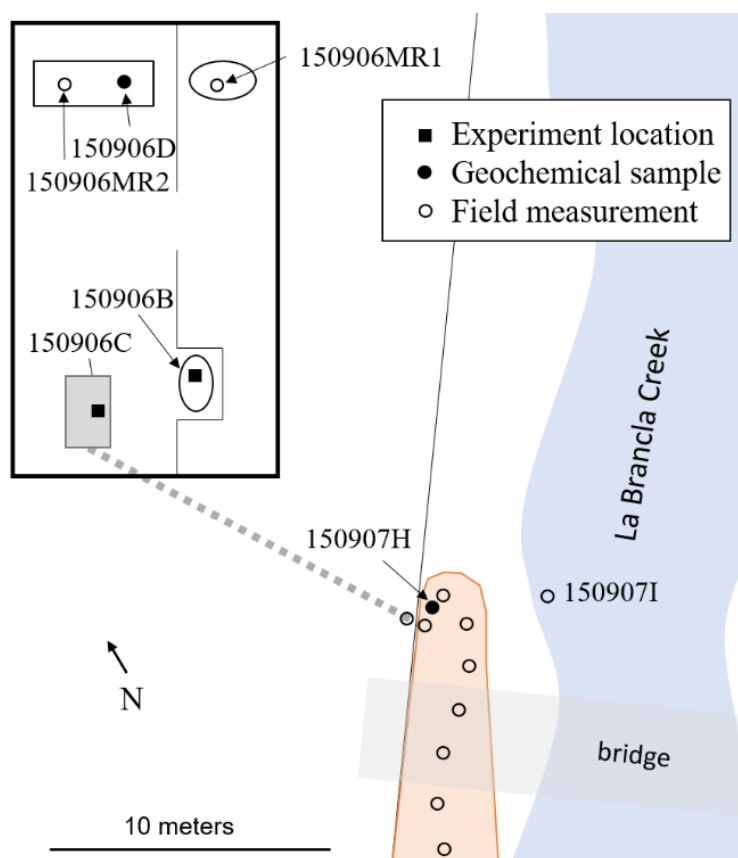


**Figure S5** – Map view of the Val Sinestra area. The top left rectangle represents the bath house where the springs originate. Springs are drawn as circles and squares, with sample locations indicated with symbols analogous to Fig S3. In addition, filled circles indicate locations with field and lab geochemical sample suites but without rate experiments. The orange area represents an iron mat located in the riverbed. The iron mat terminates abruptly when it falls down a short waterfall into the creek. The dashed line indicates an underground pipe that brings spring water from the bathhouse to the riverbed. The map is drawn to scale, except the underground pipe is truncated. A profile of solutes in the outflow of 150906C can be found in Fig S6.

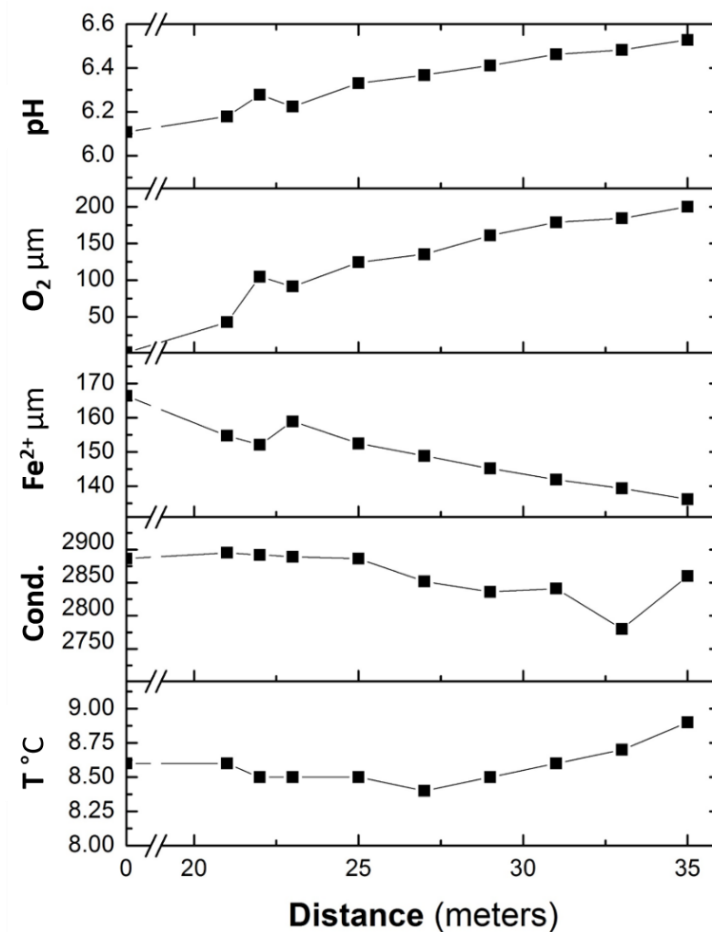


**Figure S6** – Val Sinestra outflow profile – Distance is measured from the source in the bathhouse 150906C (see map, Fig S5). The break in the distance scale corresponds to the underground pipe. The majority of the accessible outflow is located in the river bed. The pH increases with distance from the source. Dissolved oxygen increases as air infiltrates the water. The water does not reach saturation with respect to oxygen in the atmosphere despite the relatively long outflow distance. Fe<sup>2+</sup> decreases consistently along the outflow. Conductivity (μS/cm) is stable between the source and the start of the outflow but begins to decrease consistent with mineral precipitation. The temperature does not change appreciably over the distance of the outflow path.

### S2.3 Alvaneu Bad area

There are several iron and sulfide rich springs in the Alvaneu Bad area. The springs are spread over approximately a kilometer along the base of a steep slope. The outflows of the springs drain into the Albula River east of the town of Filisur and south of Alvaneu. Sampling took place at two iron springs, Arvadi and a location designated Eisenquelle. Arvadi spring is a mix of two separate springs located along a walking path next to a golf course. The source waters are contained in a locked utility building. The water is piped through a half meter diameter drainage pipe for more than 50 meters which allows interaction with the atmosphere. The pseudo-source emerges in a 4-meter diameter pool designed to look like a natural spring. The water is fully oxygenated at this point, with only minor amounts of iron remaining. The spring also contains apparent dissolved sulfide (as indicated by apparent elemental sulfur, filamentous sulfide oxidizing bacteria (*Thiothrix sp.*) and sulfide smell), which was not measured due to technical difficulties in the field. A recent study of Arvadi by Koeksoy *et al.*<sup>63</sup> measured 2.5  $\mu\text{M}$  sulfide as well as the presence of sulfide oxidizing microbes. That study also detected the presence of organisms putatively involved in iron oxidation and reduction. A profile of pH, oxygen, temperature and conductivity taken down the outflow from the pseudo-source show little change in composition over 15 meters (data in Table S20). An Fe-oxidation experiment was performed close to the pseudo-source.

Eisenquelle is an iron spring approximately 1.3 km west of the town of Filisur. This spring emerges from the base of a steep slope and produces a deeply red stained iron mat. Filamentous photosynthetic biomass is found along the length of the spring and is coated in iron oxyhydroxides, similar to the description of iron-encrusted photosynthetic biomass given by Mori *et al.*<sup>98</sup>. The flow merges with a mountain stream less than a meter from the source. Iron oxide is visible as the merged waters flow ~12 meters into the Albula river. A rate experiment was conducted at the spring source.

### S2.4 Jöri Lakes

The Jöri Lakes are a series of 24 lakes and ponds located at an altitude between approximately 2500 and 2800 meters above sea level in the Vereina valley, 10 km southeast of Davos, Switzerland. The

retreating Jöri glacier has led to an increase in the number of lakes from 13 in the early 1900's to 21 in 1999. The original 13 lakes are numbered (I – XIII) as outlined by Kreis<sup>99</sup>; the numbering was expanded to XXI by Hinder *et al.*<sup>100</sup>, and several more lakes were exposed since that publication (for example, lake XXIII sampled during this study). A topographic map of the area is shown in Fig S7. More complete descriptions of the Jöri catchment can be found in Kreis<sup>99</sup> and Hinder *et al.*<sup>100,101</sup>.

The Jöri lakes are completely covered by ice during the winter, which permits anoxic regimes that facilitate redox cycling<sup>100</sup>, and several have evidence of iron cycling<sup>53</sup>. We measured ferrous iron in waters and sediment, as well as observed widespread iron mineral staining on rocks and sediments. The snowmelt fed lakes had an extremely dilute solute concentration, with conductivities ranging from 6-50  $\mu\text{S}/\text{cm}$ . Field data collected in this area can be found in Table 2.

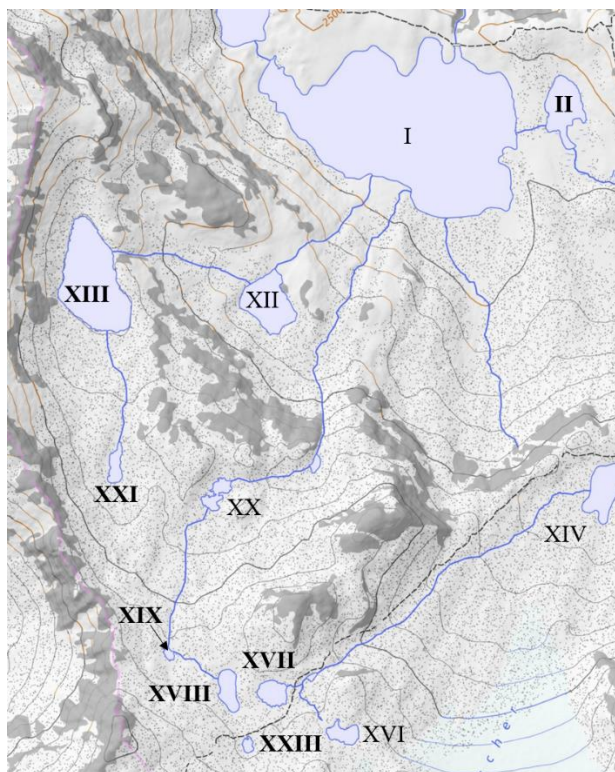


**Figure S7** – A topographical map of the western Jöri lakes catchment. Roman numerals designate lake numbers from previous publications<sup>99,100,101</sup>. Bolded numerals indicate sample locations. Lakes II, XII, XXI, and XIII have abundant iron staining on rocks. Map used with the permission of the Swiss Federal Office of Topography, Swisstopo (JA100120)

Table S7 – Field measurements from October 2012 preliminary sampling trip

Sample ID	Area	Notes	pH	Cond $\mu\text{S}$	T $^{\circ}\text{C}$	O <sub>2</sub> (aq)	Fe <sup>+2</sup>
121007A	Rablönch	same location as 150907MR2	6.3	2070	10.7	<6	60.5
121007B	Rablönch	same location as 150907MR3	6.3	2070	10.5	121	59.7
121007C	Rablönch	depleted outflow	7.9	1888	9.7	309	8.8
121007B2	Rablönch	Same location as 150907F	6.59	2070	10.7	211	ND
121007B3	Rablönch	Mid channel iron mat	7.18	2050	10.8	277	ND
121017E	Val Sinestra	Same site as 150906B	6.68	6960	7.4	106	22
121017MRA	Val Sinestra	Same site as 150906D	6.49	8700	8.8	BDL	ND
121017F	Val Sinestra	Same site 150908H	6.31	3930	8.4	60	115
121017G	Val Sinestra	Outflow in mat	6.60	3940	8.3	156	157

O<sub>2</sub> (aq) and Fe<sup>2+</sup> are  $\mu\text{molal}$

### **S3 - Field Rate Experiments**

Rate experiment data – Tables S8-S13 and Figures S8-S12 show data for experiments using the standard protocol. For each experiment, blue, red, and black points represent added Fe(II), unamended, and killed treatments, respectively. The three shapes correspond to one of three replicates for each treatment. In all cases the top figure contain the raw linear data collected and is designated a, while the bottom figure depicts the same data as natural log molal and is designated b. Tables S14-S17 and Figures S13-S15 show rate data for experiments using the rapid oxidation protocol. For each experiment, blue and black points represent the ROP-added Fe(II) and filtered treatments, respectively. The three shapes correspond to one of three replicates for each treatment. These data were used to determine rates in Table 4.

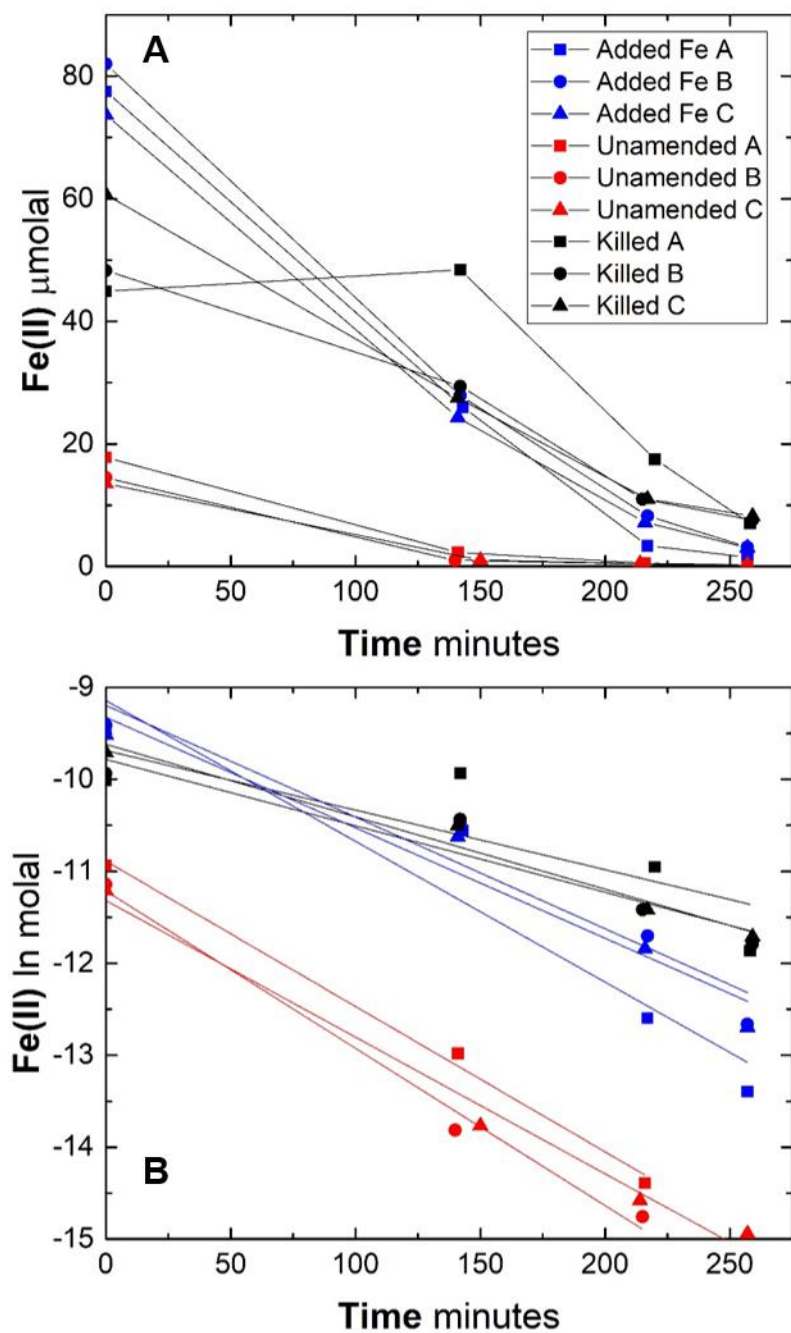
Table S8 – Raw rate experiment data for 150907F (Rablönch iron mat). See figure 1 in the full text

Type	Rep	#	Time minutes	Fe <sup>2+</sup> mg/L	Fe <sup>2+</sup> molal
Added Fe(II)	A	1	0	2.34	1.31E-04
		2	96	1.04	5.79E-05
		3	286	0.23	1.27E-05
	B	1	0	2.27	1.27E-04
		2	96	0.84	4.66E-05
		3	286	0.11	6.10E-06
	C	1	0	2.51	1.40E-04
		2	96	0.89	4.96E-05
		3	287	0.21	1.15E-05
Unamended	A	1	0	1.04	5.80E-05
		2	96	0.31	1.75E-05
		3	287	0.02	1.21E-06
	B	1	0	1.08	6.04E-05
		2	96	0.31	1.74E-05
		3	287	0.02	8.95E-07
	C	1	0	1.00	5.59E-05
		2	96	0.28	1.57E-05
		3	287	0.01	3.05E-07
Killed	A	1	0	2.23	1.24E-04
		2	96	1.13	6.30E-05
		3	287	0.37	2.08E-05
	B	1	0	2.32	1.30E-04
		2	96	1.29	7.20E-05
		3	287	0.35	1.96E-05
	C	1	0	2.23	1.25E-04
		2	96	1.11	6.18E-05
		3	288	0.38	2.11E-05



Table S9 – Raw rate experiment  
data for 150906B (Conradins springs,  
Val Sinestra)

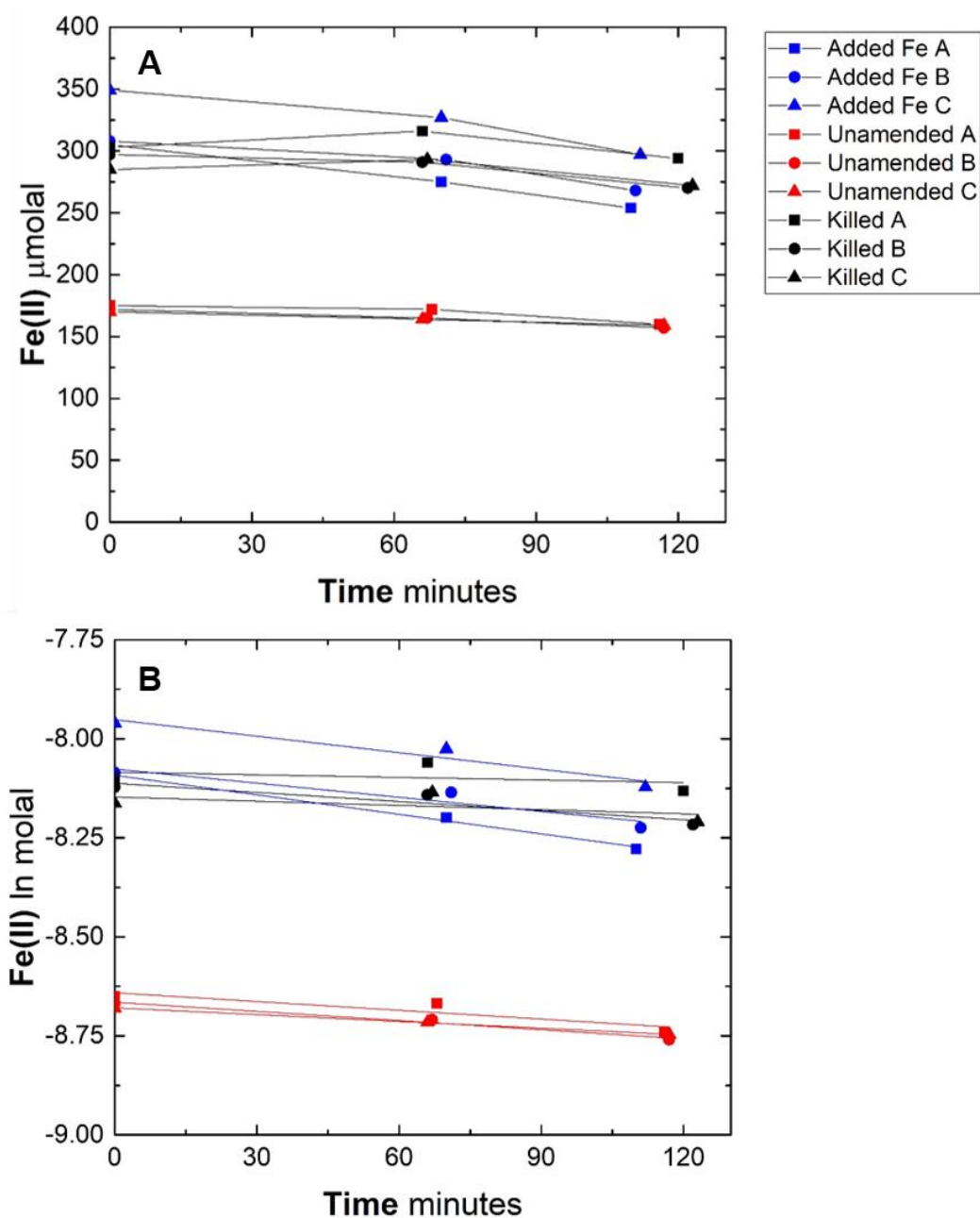
Type	Rep	#	Time minutes	Fe <sup>2+</sup> mg/L	Fe <sup>2+</sup> Molal
Added Fe(II)	A	1	0	1.39	7.75E-05
		2	143	0.47	2.60E-05
		3	217	0.06	3.38E-06
		4	257	0.03	1.52E-06
	B	1	0	1.47	8.20E-05
		2	142	0.50	2.79E-05
		3	217	0.15	8.26E-06
		4	257	0.10	3.16E-06
	C	1	0	1.32	7.37E-05
		2	141	0.43	2.43E-05
		3	216	0.13	7.21E-06
		4	257	0.10	3.06E-06
Unamended	A	1	0	0.32	1.78E-05
		2	141	0.04	2.30E-06
		3	216	0.01	5.62E-07
		4	257	BDL	BDL
	B	1	0	0.26	1.45E-05
		2	140	0.02	1.00E-06
		3	215	0.01	3.90E-07
		4	257	BDL	BDL
	C	1	0	0.24	1.35E-05
		2	150	0.02	1.05E-06
		3	214	0.01	4.67E-07
		4	257	0.01	3.24E-07
Killed	A	1	0	0.80	4.49E-05
		2	142	0.87	4.84E-05
		3	220	0.31	1.75E-05
		4	258	0.13	7.05E-06
	B	1	0	0.86	4.83E-05
		2	142	0.53	2.94E-05
		3	215	0.20	1.10E-05
		4	259	0.14	7.57E-06
	C	1	0	1.09	6.07E-05
		2	141	0.49	2.75E-05
		3	217	0.20	1.10E-05
		4	259	0.15	8.20E-06



**Figure S8** - Iron oxidation experimental results for 150906B Conradins Springs at Val Sinestra, using the standard rate experiment protocol.. Plot S8a shows data as collected during field experiments. The added Fe(II) (blue) and killed (black) points both have added ferrous iron, which is why the initial concentration is higher than the unamended (red) points. Fig S8b shows the same data plotted on a natural logarithmic scale. Lines reflect linear fits that are indicative of the rate constant.

Table S10 – Raw rate experiment data for  
150906C, Trap door spring at Val Sinestra

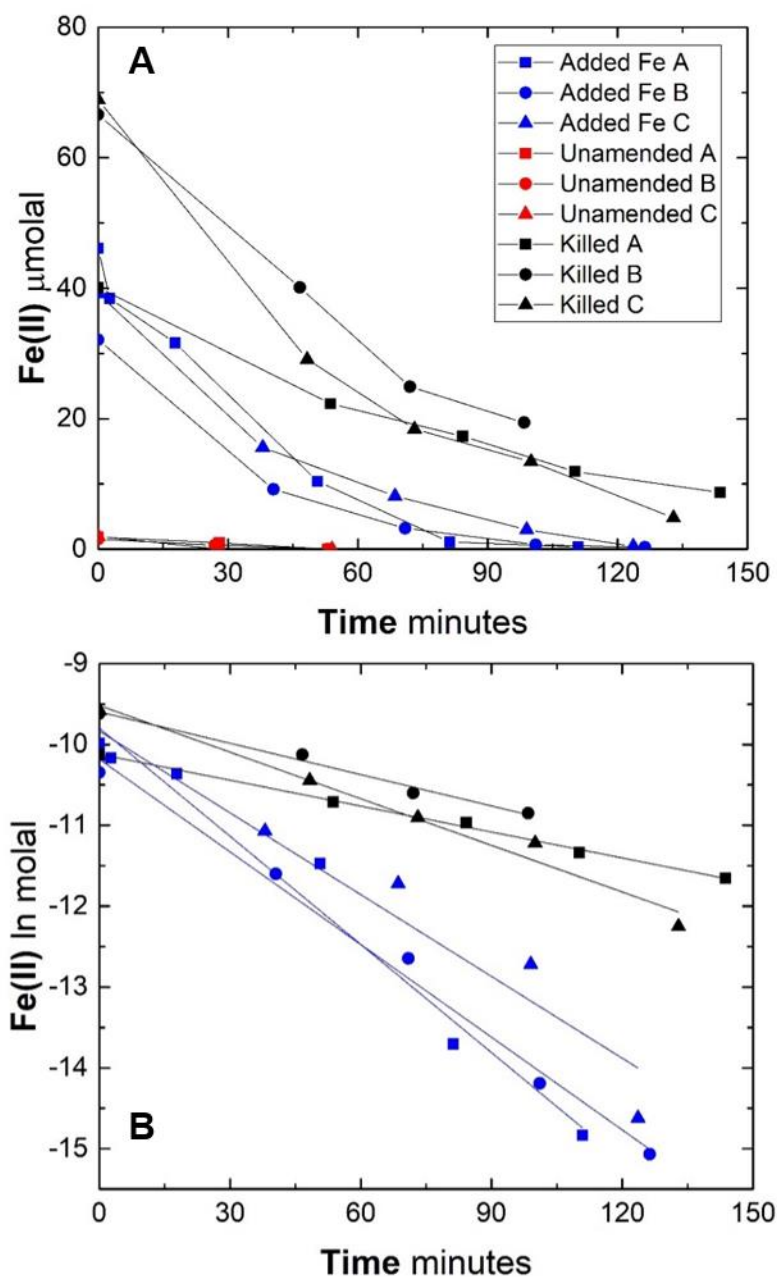
Type	Rep	#	Time minutes	Fe <sup>2+</sup> mg/L	Fe <sup>2+</sup> molal
Added Fe(II)	A	1	0	5.39	3.05E-04
		2	70	4.92	2.75E-04
		3	110	4.56	2.54E-04
	B	1	0	5.52	3.08E-04
		2	71	5.25	2.93E-04
		3	111	4.79	2.68E-04
	C	1	0	6.24	3.49E-04
		2	70	5.85	3.27E-04
		3	112	5.32	2.97E-04
Unamended	A	1	0	3.14	1.75E-04
		2	68	3.08	1.72E-04
		3	116	2.87	1.60E-04
	B	1	0	3.08	1.72E-04
		2	67	2.96	1.65E-04
		3	117	2.82	1.57E-04
	C	1	0	3.04	1.70E-04
		2	66	2.94	1.64E-04
		3	117	2.84	1.59E-04
Killed	A	1	0	5.43	3.03E-04
		2	66	5.66	3.16E-04
		3	120	5.26	2.94E-04
	B	1	0	5.31	2.97E-04
		2	66	5.21	2.91E-04
		3	122	4.83	2.70E-04
	C	1	0	5.10	2.85E-04
		2	67	5.25	2.93E-04
		3	123	4.87	2.72E-04



**Figure S9** – Iron oxidation experimental results for 150906C trap door spring at Val Sinestra, using the standard rate experiment protocol.. Plot S9a shows data as collected during field experiments. The added Fe(II) (blue) and killed (black) points both have added ferrous iron, which is why the initial concentration is higher than the unamended (red) points. Plot S9b shows the same data plotted on a natural logarithmic scale. Lines reflect linear fits that are indicative of the rate constant.

Table S11 – Raw rate experiment data for  
150911T Eisenquelle (Alvaneu Bad)

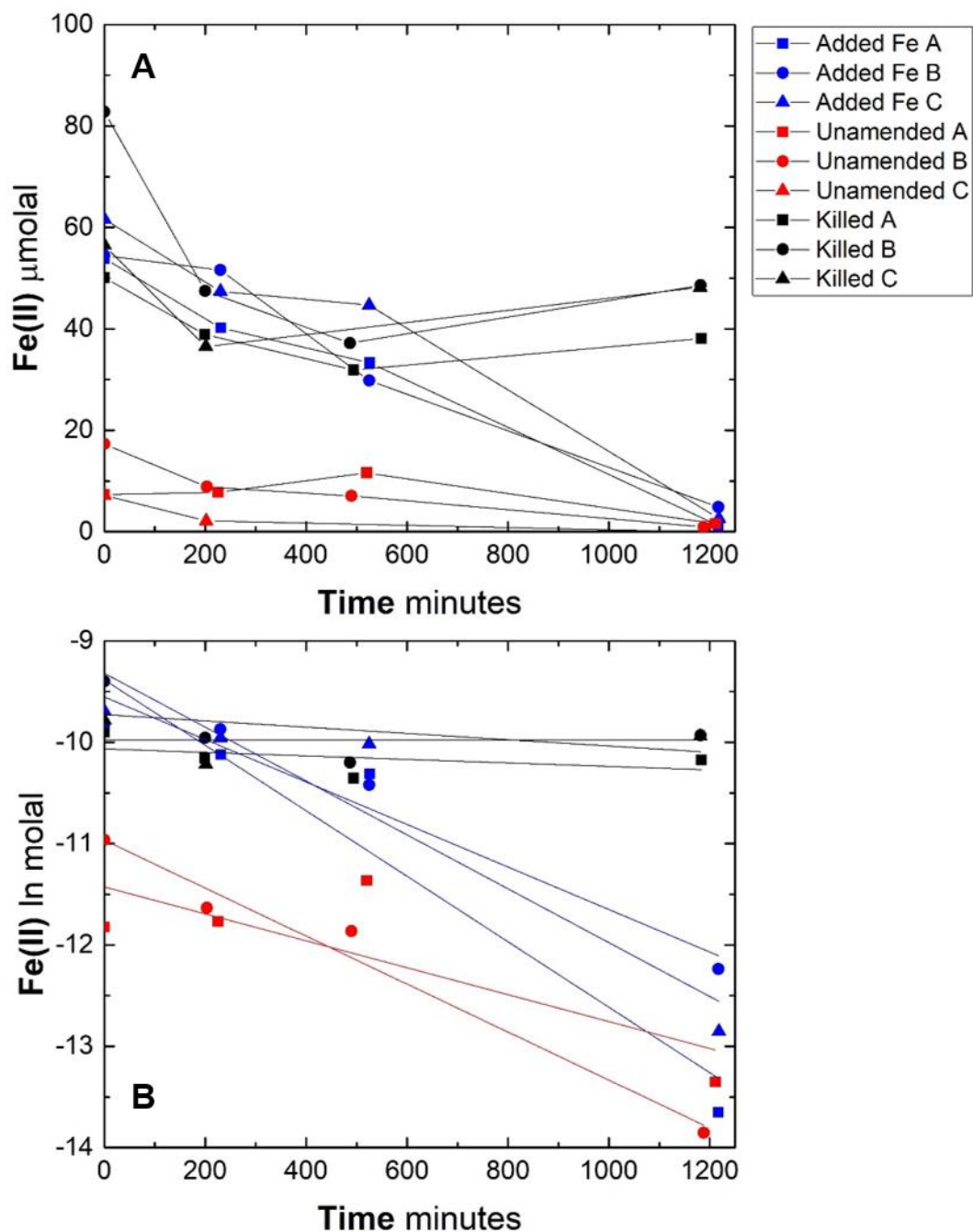
Type	Rep	#	Time minutes	Fe <sup>2+</sup> mg/L	Fe <sup>2+</sup> molal
Added Fe(II)	A	1	0.0	0.83	4.61E-05
		2	2.7	0.69	3.84E-05
		3	17.8	0.57	3.16E-05
		4	50.7	0.19	1.04E-05
		5	81.2	0.02	1.12E-06
		6	110.9	0.01	3.62E-07
	B	1	0.0	0.58	3.21E-05
		2	40.5	0.16	9.17E-06
		3	70.9	0.06	3.22E-06
		4	101.1	0.01	6.86E-07
		5	126.3	0.01	2.86E-07
	C	1	0.0	0.70	3.92E-05
		2	38.0	0.28	1.56E-05
		3	68.6	0.15	8.14E-06
		4	99.0	0.1	3.00E-06
		5	123.6	0.0	4.48E-07
Unamended	A	1	0	0.10	1.83E-06
		2	28	0.05	9.81E-07
		3	53	BDL	BDL
	B	1	0	0.09	1.54E-06
		2	27	0.04	6.29E-07
		3	53	BDL	BDL
	C	1	0	0.11	1.94E-06
		2	28	BDL	BDL
		3	54	BDL	BDL
Killed	A	1	0.0	0.72	4.01E-05
		2	53.7	0.40	2.23E-05
		3	84.2	0.31	1.73E-05
		4	110.1	0.21	1.19E-05
		5	143.7	0.16	8.70E-06
	B	1	0.0	1.19	6.66E-05
		2	46.6	0.72	4.01E-05
		3	72.0	0.45	2.49E-05
		4	98.4	0.35	1.94E-05
	C	1	0.0	1.23	6.89E-05
		2	48.3	0.52	2.91E-05
		3	73.1	0.33	1.84E-05
		4	100.0	0.24	1.34E-05
		5	132.9	0.09	4.79E-06



**Figure S10** –Iron oxidation experimental results for 150911T Eisenquelle spring at Alvaneu Bad, using the standard rate experiment protocol. Plot S10a shows data as collected during field experiments. The added Fe(II) (blue) and killed (black) points both have added ferrous iron, which is why the initial concentration is higher than the unamended (red) points. Plot S10b shows the same data plotted on a natural logarithmic scale. The unamended experiment was depleted of iron after the second measurement and was not included in rate constant determination. Lines reflect linear fits that are indicative of the rate constant.

Table S12 – Raw rate experiment data for  
150909K, Jöri Lake XIII

Type	Rep	#	Time minutes	Fe <sup>2+</sup> mg/L	Fe <sup>2+</sup> molal
Added Fe(II)	A	1	0	0.96	5.39E-05
		2	231	0.72	4.02E-05
		3	526	0.60	3.33E-05
		4	1217	0.02	1.18E-06
	B	1	0	0.98	5.45E-05
		2	230	0.92	5.16E-05
		3	525	0.53	2.98E-05
		4	1217	0.09	4.85E-06
	C	1	0	1.10	6.16E-05
		2	230	0.85	4.74E-05
		3	525	0.80	4.47E-05
		4	1218	0.05	2.62E-06
Unamended	A	1	0	0.13	7.33E-06
		2	225	0.14	7.75E-06
		3	520	0.21	1.16E-05
		4	1211	0.03	1.59E-06
	B	1	0	0.31	1.73E-05
		2	203	0.16	8.86E-06
		3	490	0.13	7.05E-06
		4	1188	0.02	9.62E-07
	C	1	0	0.13	7.18E-06
		2	202	0.04	2.11E-06
		3	1188	BDL	BDL
		4		BDL	BDL
Killed	A	1	0	0.90	5.01E-05
		2	199	0.70	3.89E-05
		3	494	0.57	3.19E-05
		4	1183	0.56	3.81E-05
	B	1	0	1.11	8.28E-05
		2	200	0.85	4.75E-05
		3	487	0.67	3.72E-05
		4	1182	0.57	4.86E-05
	C	1	0	1.01	5.65E-05
		2	201	0.65	3.65E-05
		3	1181	0.63	4.82E-05



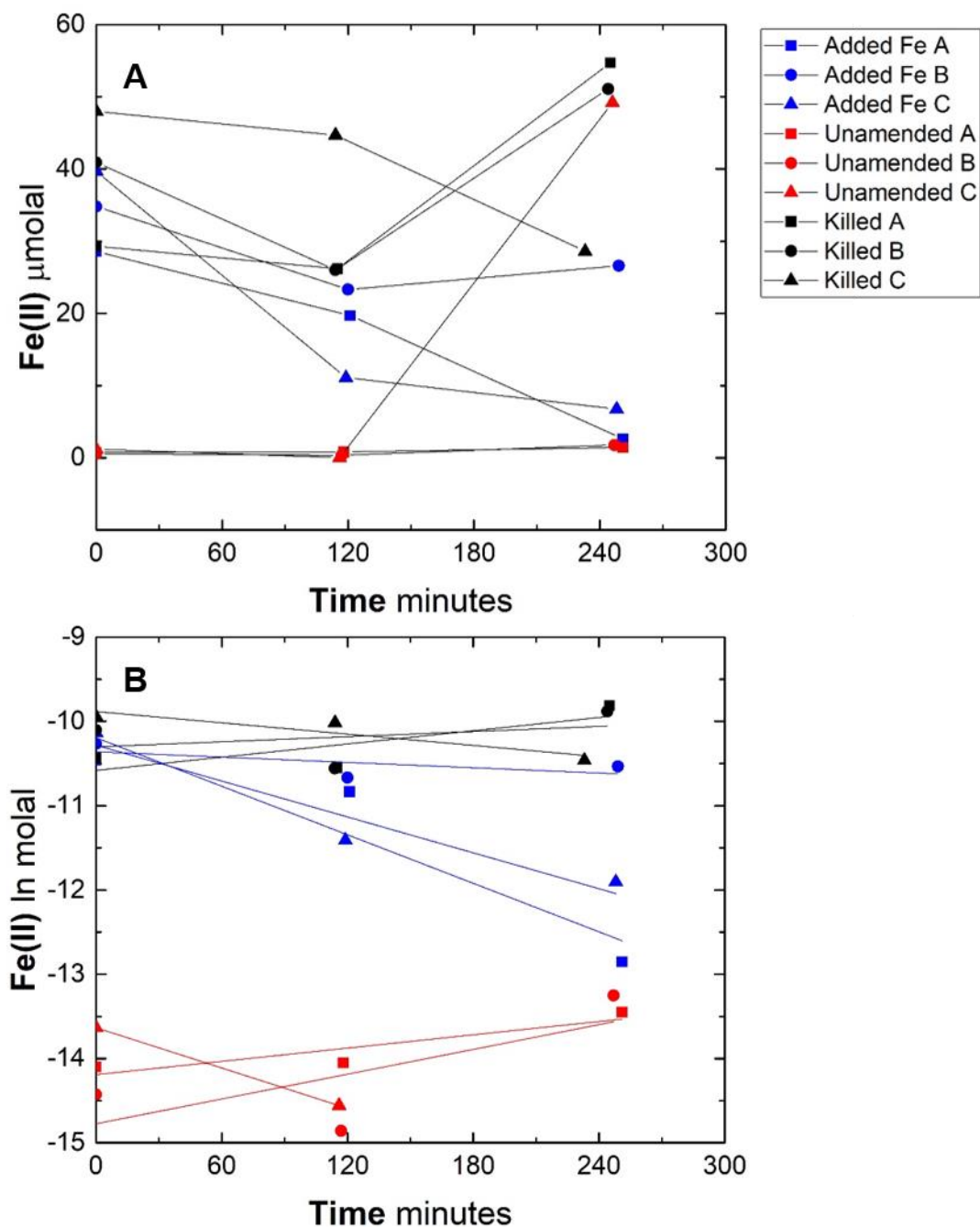
**Figure S11** –Iron oxidation experimental results for 150909K Jöri lake XIII at 10 meters depth, using the standard rate experiment protocol. Plot S11a shows data as collected during field experiments. The added Fe(II) (blue) and killed (black) points both have added ferrous iron, which is why the initial concentration is higher than the unamended (red) points. Plot S11b shows the same data plotted on a natural logarithmic scale. Lines reflect linear fits that are indicative of the rate constant.



Table S13 – Raw rate experiment data for  
150910O (Jöri lake II)

Type	Rep	#	Time minutes	Fe <sup>2+</sup> mg/L	Fe <sup>2+</sup> molal
Added Fe(II)	A	1	0	0.51	2.86E-05
		2	121	0.35	1.97E-05
		3	251	0.05	2.62E-06
	B	1	0	0.62	3.48E-05
		2	120	0.42	2.33E-05
		3	249	0.48	2.66E-05
	C	1	0	0.71	3.97E-05
		2	119	0.20	1.11E-05
		3	250	0.12	6.75E-06
Unamended	A	1	0	0.01	7.52E-07
		2	118.0	0.01	7.90E-07
		3	251	0.03	1.44E-06
	B	1	0	0.01	5.43E-07
		2	117	0.01	3.52E-07
		3	247	0.03	1.76E-06
	C	1	0	0.02	1.20E-06
		2	116	0.00	4.76E-07
		3	246	0.88	4.92E-05*
Killed	A	1	0	0.52	2.93E-05
		2	115	0.47	2.62E-05
		3	245	0.98	5.47E-05
	B	1	0	0.73	4.09E-05
		2	114	0.47	2.60E-05
		3	244	0.92	5.11E-05
	C	1	0	0.86	4.80E-05
		2	114	0.80	4.47E-05
		3	233	0.51	2.86E-05

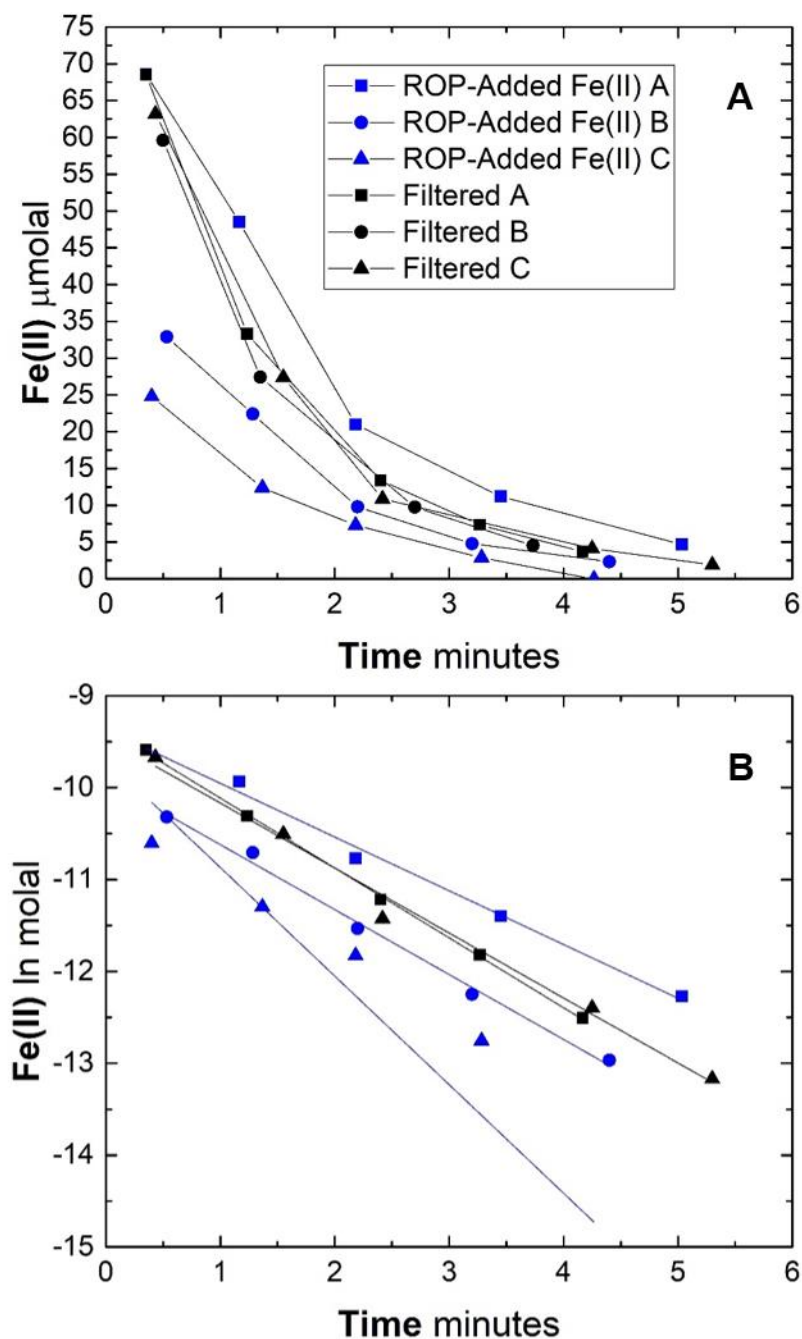
\* outlier omitted in rate analysis



**Figure S12** –Iron oxidation experimental results for 1509100 Jöri lake II at 10 meters depth, using the standard rate experiment protocol. Plot S12a shows data as collected during field experiments. The added Fe(II) (blue) and killed (black) points both have added ferrous iron, which is why the initial concentration is higher than the unamended (red) points. Plot S12b shows the same data plotted on a natural logarithmic scale. Lines reflect linear fits that are indicative of the rate constant.

Table S14 – Raw rate experiment data for  
150908J (Rablönch outflow)

Type	Rep	#	Time seconds	Fe <sup>2+</sup> mg/L	Fe <sup>2+</sup> molal
Added Fe(II)	A	1	21	1.23	6.86E-05
		2	70	0.87	4.85E-05
		3	131	0.38	2.10E-05
		4	207	0.20	1.12E-05
		5	302	0.08	4.68E-06
	B	1	32	0.59	3.29E-05
		2	77	0.40	2.24E-05
		3	132	0.18	9.80E-06
		4	192	0.09	4.79E-06
		5	264	0.04	2.34E-06
	C	1	24	0.44	2.48E-05
		2	82	0.22	1.24E-05
		3	131	0.13	7.30E-06
		4	197	0.1	2.89E-06
		5	256	BDL	BDL
Filtered	A	1	21	1.23	6.85E-05
		2	74	0.60	3.33E-05
		3	144	0.24	1.34E-05
		4	196	0.13	7.36E-06
		5	250	0.07	3.70E-06
	B	1	30	1.07	5.96E-05
		2	81	0.49	2.74E-05
		3	162	0.17	9.77E-06
		4	224	0.08	4.52E-06
	C	1	26	1.13	6.32E-05
		2	93	0.49	2.74E-05
		3	145	0.20	1.09E-05
		4	255	0.07	4.13E-06
		5	318	0.03	1.91E-06



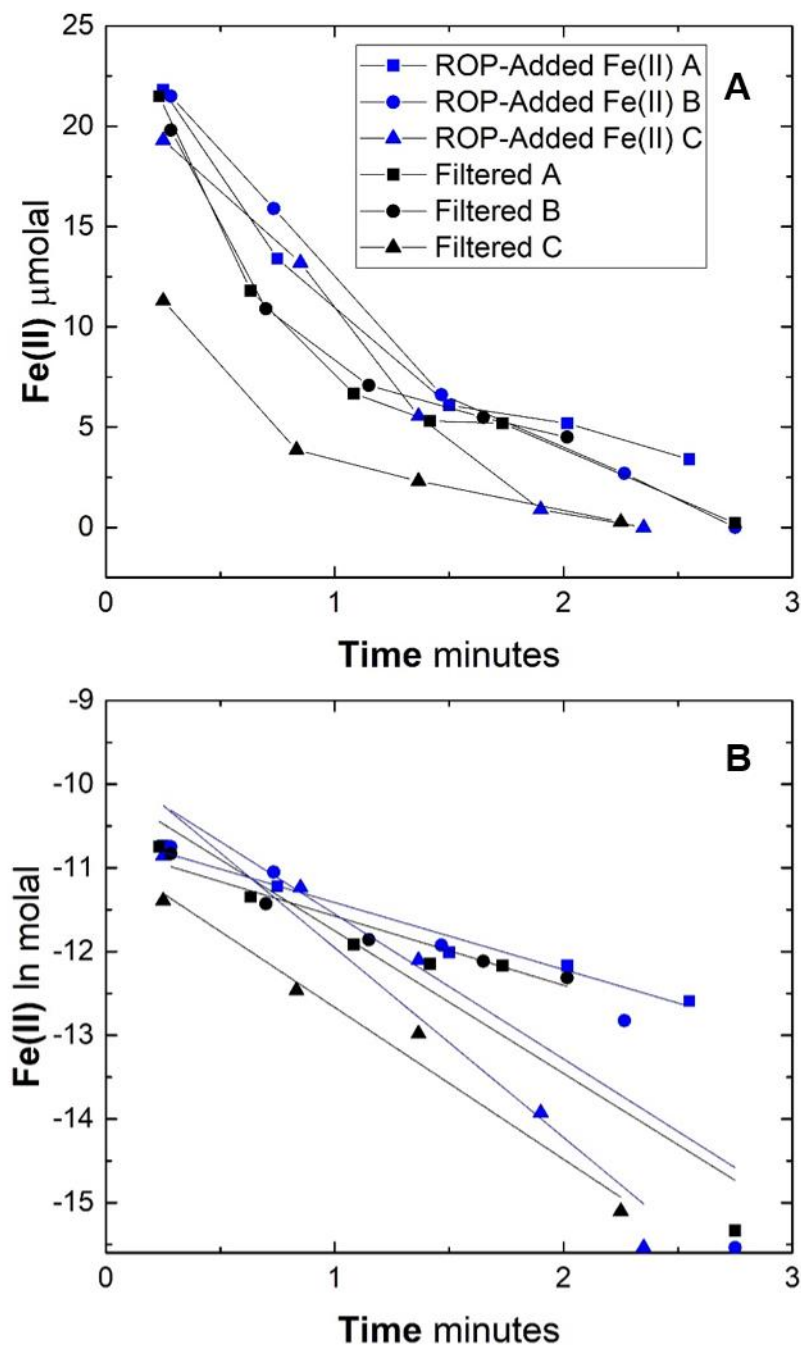
**Figure S13** – Iron oxidation experimental results for 150908J, an outflow at Rablönch spring, using the rapid oxidation protocol. Blue points represent the ROP-added Fe(II) replicates, while black points indicate the filtered (abiotic) treatments. Time is started when the  $\text{Fe}^{2+}$  reagent is added, while the first measurement is made immediately after. Fig S13a shows data as collected during field experiments. Both data sets have added ferrous iron. Fig S13b shows the same data but plotted on a natural logarithmic scale, revealing the first order kinetics of the reaction. Lines reflect linear fits that are indicative of the rate constant.

Table S15 – Raw rate experiment data for  
150907G, Rablönche Outflow See Figure 2  
in the full text of this paper for plots of these data.

Type	Rep	#	Time seconds	Fe <sup>2+</sup> mg/L	Fe <sup>2+</sup> molal
Added Fe(II)	A	1	30	0.67	3.74E-05
		2	123	0.14	7.96E-06
		3	235	0.03	1.70E-06
	B	1	20	0.63	3.54E-05
		2	60	0.22	1.24E-05
		3	122	0.10	5.40E-06
		4	170	0.05	3.05E-06
	C	1	16	1.07	5.96E-05
		2	52	0.48	2.70E-05
		3	107	0.15	8.50E-06
		4	147	0.08	4.38E-06
		5	193	0.05	2.95E-06
Filtered	A	1	16	0.83	4.66E-05
		2	43	0.48	2.67E-05
		3	72	0.25	1.40E-05
		4	112	0.10	5.58E-06
		5	148	0.04	2.05E-06
	B	1	14	1.01	5.63E-05
		2	49	0.38	2.10E-05
		3	80	0.20	1.12E-05
		4	115	0.08	4.70E-06
		5	150	0.05	2.54E-06
	C	1	12	1.01	5.62E-05
		2	48	0.42	2.33E-05
		3	93	0.15	8.58E-06
		4	130	0.06	3.30E-06
		5	164	0.04	2.09E-06

Table S16 – Raw rate experiment data for  
150905A (Arvadi Spring, Alvaneu Bad)

Type	Rep	#	Time seconds	Fe <sup>2+</sup> mg/L	Fe <sup>2+</sup> molal
Added Fe(II)	A	1	15	1.22	2.18E-05
		2	45	0.75	1.34E-05
		3	90	0.34	6.09E-06
		4	121	0.29	5.19E-06
		5	153	0.19	3.40E-06
	B	1	17	1.20	2.15E-05
		2	44	0.89	1.59E-05
		3	88	0.37	6.62E-06
		4	136	0.15	2.69E-06
		5	165	BDL	BDL
	C	1	15	1.08	1.93E-05
		2	51	0.74	1.32E-05
		3	82	0.31	5.55E-06
		4	114	0.05	8.95E-07
		5	141	BDL	BDL
Filtered	A	1	14	1.20	2.15E-05
		2	38	0.66	1.18E-05
		3	65	0.37	6.68E-06
		4	85	0.30	5.30E-06
		5	104	0.29	5.19E-06
		6	165	0.01	2.19E-07
	B	1	17	1.11	1.98E-05
		2	42	0.61	1.09E-05
		3	69	0.40	7.08E-06
		4	99	0.31	5.48E-06
		5	121	0.25	4.50E-06
	C	1	15	0.63	1.13E-05
		2	50	0.22	3.87E-06
		3	82	0.13	2.31E-06
		4	135	0.02	2.76E-07



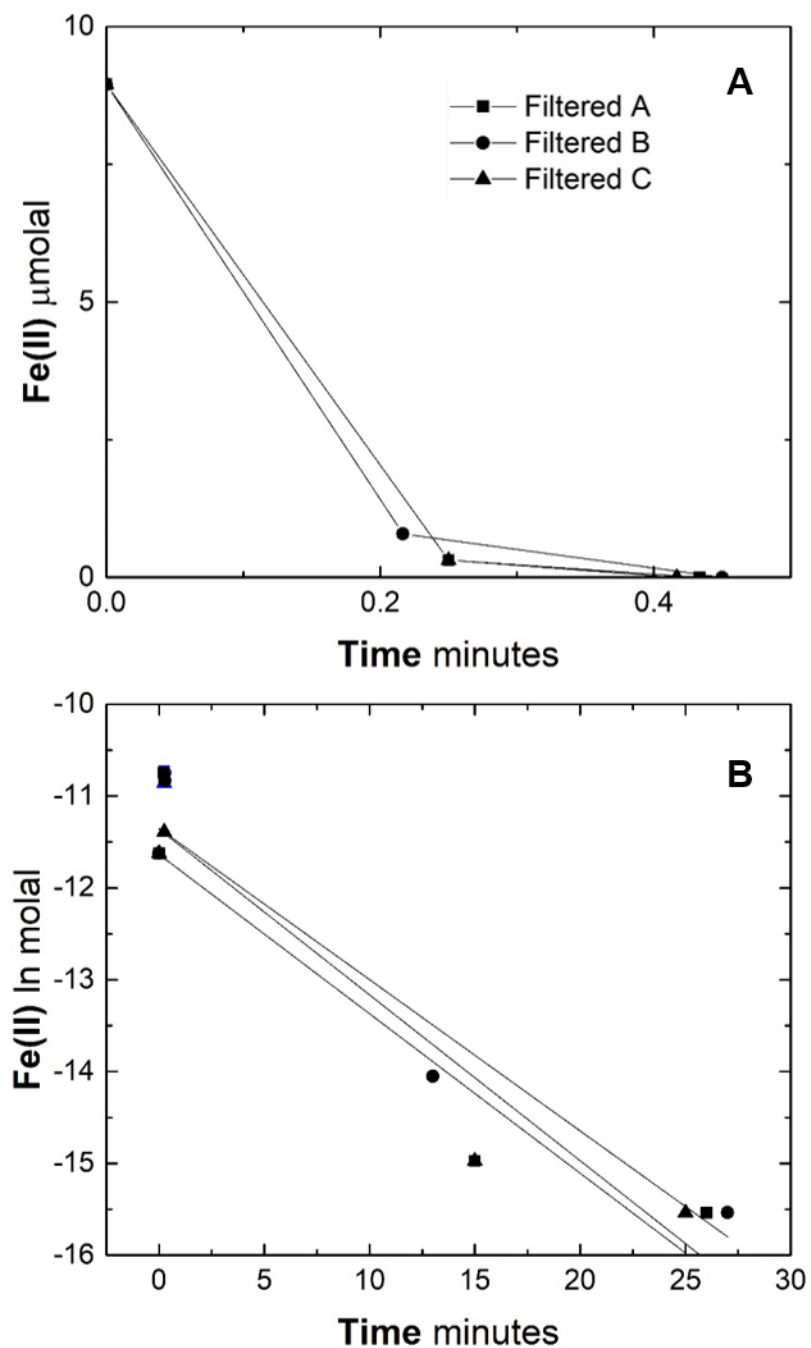
**Figure S14** – Iron oxidation experimental results for 150905A, Arvadi spring at Alvaneu bad, using the rapid oxidation protocol. Blue points represent the ROP-added Fe(II) replicates, while black points indicate the filtered (abiotic) treatments. Fig S14a shows data as collected during field experiments. Both data sets have added ferrous iron. Fig S14b shows the same data but plotted on a natural logarithmic scale, revealing the first order kinetics of the reaction. Lines reflect linear fits that are indicative of the rate constant.

Table S17 – Raw rate experiment data for  
150909M, Jöri Lake XX.

Type	Rep	#	Time seconds	Fe <sup>2+</sup> mg/L	Fe <sup>2+</sup> molal
Filtered spring water	A	1	0	0.5 <sup>#</sup>	8.95E-06 <sup>#</sup>
		2	15	0.02	3.14E-07
		3	26	BDL	BDL
	B	1	0	0.5 <sup>#</sup>	8.95E-06 <sup>#</sup>
		2	13	0.04	7.90E-07
		3	27	BDL	BDL
	C	1	0	0.5 <sup>#</sup>	8.95E-06 <sup>#</sup>
		2	15	0.02	3.14E-07
		3	25	BDL	BDL

<sup>#</sup> indicates the concentration of added Fe(II) at T=0, which assumes all Fe(II) is from added reagents. Fe<sup>2+</sup> measurements in this experiment are all at or below the detection limit by the second measurement point. The rates calculated in table 4 are minimum rates determined by assuming the 0.5 mg / L ferrous iron is all depleted in 30 seconds.





**Figure S15** – Iron oxidation experimental results for 150909M, Jöri Lake XX, using the rapid oxidation protocol. Results are only reported for the Filtered treatment, as Fe(II) fell below the detection limit in seconds. Fig S15a shows data as collected during field experiments. Fig S15b shows the same data but plotted on a natural logarithmic scale. The third datapoint of each replicate is below the detection limit.

## S4 Supplementary geochemical data

Table S18 - Rablönch outflow profile (from Fig S4)

Distance meters	pH	T °C	Conductivity μS / cm	oxygen μmolal	Fe (II) μmolal
0 (150907F)	6.32	11.1	1674	162	93.2
2	6.38	11.0	1600	198	89.0
4	6.60	11.0	1560	228	77.2
6	6.63	11.0	1668	245	72.5
8	6.85	11.6	1675	274	56.5
10	7.12	12.1	1685	298	48.1
12	7.42	11.3	1628	313	35.3
14	7.60	11.3	1315	315	21.2
16	7.62	11.0	1350	315	15.7
18	7.66	11.0	1408	318	12.0
20	7.70	10.7	1386	318	3.4

Table S19 – Val Sinestra outflow profile (from Fig S6)

Distance meters	pH	T °C	Conductivity μS / cm	oxygen μmolal	Fe (II) μmolal
0 (150906C)	6.11	8.6	2886	1.4	166
21	6.179	8.5	2895	43	154.7
23	6.2239	8.4	2889	91	159.0
25	6.33	8.4	2886	124	152.5
27	6.368	8.4	2852	135	148.9
29	6.412	8.5	2836	161	145.2
31	6.463	8.5	2841	179	141.9
33	6.483	8.4	2780	184	139.4
35	6.528	8.2	2860	200	136.2

Table S20 - Arvadi Outflow profile

Distance Meters	pH	T °C	Conductivity μS / cm	oxygen μmolal	Fe (II) μmolal
0 (150905A)	7.93	7.8	1118	314	2.5
5	8.033	7.8	1116	313	2.0
8	8.048	7.8	1118	313	1.8
11	8.051	7.8	1117	313	1.8
14	8.068	7.9	1118	314	1.6
17	8.066	7.8	1118	314	1.6
20	8.082	7.9	959	316	1.6

Table S21 – Calculated species abundance (all values log molal). Values in this table used in Fig 6b

Sample ID	Fe <sup>2+</sup>	FeCO <sub>3</sub> (aq)	FeHCO <sub>3</sub> <sup>+</sup>	Fe(CO <sub>3</sub> ) <sub>2</sub> <sup>-2</sup>	FeSO <sub>4</sub> (aq)	FeOH <sup>+</sup>	Fe(OH) <sub>2</sub>	FeCl <sup>+</sup>	FeF <sup>+</sup>
150905A	-6.07	-5.92	-7.33	-8.84	-6.40	-8.20		-11.29	-8.99
150911T	-5.57	-6.32	-7.13	-10.07	-5.76	-8.32		-10.70	-8.58
150906B	-4.22	-4.45	-4.51	-7.48	-5.14	-7.75	-15.35	-6.34	-7.74
150906C	-3.94	-4.96	-4.54	-8.98	-4.94	-7.89		-6.31	-7.48
150906D	-6.35	-6.18	-6.61	-8.76	-7.18	-9.50		-8.35	-9.71
150908H	-4.10	-4.44	-4.54	-7.74	-5.15	-7.55	-7.74	-6.49	-7.69
150907F	-4.22	-4.87	-4.68	-8.58	-5.84	-7.87		-7.71	-8.13
150907G	-6.64	-5.74	-7.14	-7.92	-8.22	-8.70		-10.09	-10.27
150908J	-5.36	-4.65	-5.83	-7.03	-6.98	-7.60		-8.82	-9.32
150909N	-4.81	-7.33	-7.44		-7.53	-8.16		-10.61	-8.54

Blank values indicate species abundance is < 10<sup>-17</sup> molal

Table S22 – Organic acid abundances for swiss springs and lakes

Sample	formate ppb	stdev	Lactate ppb	stdev	acetate ppb	stdev
150905A	55.6	0.0	BDL		BDL	
150911T	BDL		BDL		BDL	
150906B	BDL		37.9	4.2	BDL	
150906C	BDL		BDL		BDL	
150906D	9.3	0.0	29.5	0.0	BDL	
150908H	BDL		BDL		BDL	
150907F	8.9	1.1	BDL		BDL	
150907G	BDL		10.5	2.1	BDL	
150908J	BDL		BDL		BDL	
150909K	BDL		BDL		BDL	
150909L	BDL		BDL		BDL	
150909M	BDL		BDL		BDL	
150909N	BDL		16.8	4.2	10.5	3.5
150910O	39.7	7.7	BDL		BDL	
150910P	BDL		BDL		BDL	
150910Q	BDL		BDL		BDL	
150910R	BDL		BDL		BDL	
150910S	BDL		BDL		BDL	

BDL – Below Detection Limit. Detection limits are approximately 8 ppb for formate, and 10 ppb for lactate and acetate.

Table S23 -  $\delta^{18}\text{O}$  and  $\delta^2\text{H}$  water isotope values for sample locations

Sample ID	Sample location or description	$\delta^{18}\text{O}$		$\delta^2\text{H}$	
		vVSMOW	Std Dev	vVSMOW	Std Dev
150905A	Arvadi	-12.34	0.10	-89.82	0.10
150911T	Eisenquelle	-14.28	0.10	-104.80	0.44
MR	Pipe at Eisenquelle	-14.20	0.04	-100.85	0.21
150911V3	Albula River	-13.37	0.08	-94.71	0.29
150911V1	Mountain stream	-13.81	0.08	-98.33	0.47
150911V4	Mountain runoff	-13.65	0.05	-98.69	0.15
150906B	Conradins	-12.86	0.05	-100.58	0.42
150906C	Unnamed spring	-12.67	0.06	-99.97	0.61
150906D	Ulrichs pool	-12.14	0.09	-98.03	0.75
150908H	Outflow from 150906C	-13.50	0.01	-103.41	0.26
150907F	Rablönch iron mat	-14.25	0.06	-108.20	0.53
150907G	Rablönch minimal staining	-13.93	0.04	-107.42	0.22
150908J	Rablönch iron stained	-14.36	0.10	-108.83	0.48
150909K	Jöri Lake XIII	-13.31	0.08	-97.08	0.87
150909L	Jöri Lake XII Outflow	-13.30	0.08	-97.24	0.60
150909M	Jöri Lake XXI	-12.19	0.10	-84.93	1.42
150909N	Jöri Lake XIII 10m Depth	-14.14	0.09	-101.16	0.48
150910O	Jöri Lake II	-13.59	0.08	-96.61	0.86
MR	Jöri Lake I	-12.96	0.06	-94.24	0.35
MR	Jöri Lake XII	-12.66	0.06	-92.94	0.11
150910P	Snow above Jöri lake XIII	-11.27	0.10	-76.20	0.27
150910V5	Jöri Lake XVII	-11.06	0.06	-81.78	0.26

## S5 – Microbial community data

Tables S24 through S27 present OTU identity as determined by manual BLASTn searches of the NCBI 16s ribosomal RNA sequence library. Note that results in these tables are similar, but not always identical, to results using the Silva database. Notably, some sequences identified as *Sideroxydans* by the NCBI database are identified as *Gallionella* by the Silva database. The species is always included for reference, but should not be considered accurate if sequence similarity is < 97%. Identities below 90% should be considered provisional.

Table S24 - OTU sequence identity of organisms at Rablönch sample locations  $\geq 1\%$  abundance

Sample	Sequence Abundance	Identity	Sequence similarity
<b>150907F</b> iron mat	21.1%	<i>Gallionella capsiferriformans</i>	97%
	7.0%	<i>Acidovorax valerianellae</i>	100%
	2.3%	<i>Bacteriovorax stolpii</i>	98%
	2.2%	<i>Rhodobacter sediminis</i>	99%
	1.7%	<i>Gallionella capsiferriformans</i>	97%
	1.7%	<i>Sideroxydans lithotrophicus</i>	99%
	1.5%	<i>Porphyrobacter colymbi</i>	100%
	1.3%	<i>Rhodoferrax antarcticus</i>	98%
	1.3%	<i>Gemmobacter tilapia</i>	99%
	1.0%	<i>Hydrogenophaga caeni</i>	100%
	1.0%	<i>Methylobium petroleiphilum</i>	99%
	1.0%	<i>Sediminibacterium salmoneum</i>	99%
<b>150908J</b> Iron stained terrace	10.74%	<i>Acidovorax valerianellae</i>	100%
	4.23%	<i>Rhodobacter sediminis</i>	99%
	2.57%	<i>Gallionella capsiferriformans</i>	97%
	2.45%	<i>Novosphingobium lentum</i>	99%
	2.23%	<i>Oscillochloris trichoides</i>	88%
	2.14%	<i>Rhodoferrax antarcticus</i>	98%
	1.96%	<i>Lacihabitans soyangensis</i>	100%
	1.87%	<i>Gemmobacter tilapia</i>	99%
	1.72%	<i>Terrimonas crocea</i>	99%
	1.31%	<i>Salinibacterium xinjiangense</i>	100%
	1.28%	<i>Tychonema bourrellyi</i>	100%
	1.25%	<i>Thiobacillus thioparus</i>	95%
	1.09%	<i>Hyphomonas polymorpha</i>	98%
	1.08%	<i>Brevundimonas denitrificans</i>	100%
	1.03%	<i>Devosia submarina</i>	99%
<b>150907G</b> minimal iron staining	7.54%	<i>Acidovorax valerianellae</i>	100%
	3.11%	<i>Rhodobacter sediminis</i>	99%
	2.86%	<i>Lacihabitans soyangensis</i>	100%
	2.16%	<i>Novosphingobium lentum</i>	99%
	2.14%	<i>Terrimonas crocea</i>	99%
	2.02%	<i>Oscillochloris trichoides</i>	88%
	1.43%	<i>Brevundimonas denitrificans</i>	100%
	1.41%	<i>Carboxydotherrmus ferrireducens</i>	81%
	1.40%	<i>Ferruginibacter paludis</i>	95%
	1.29%	<i>Tychonema bourrellyi</i>	100%
	1.29%	<i>Pseudomonas syringae</i>	100%
	1.23%	<i>Gemmobacter tilapia</i>	99%

1.19%	<i>Rhizobium azooxidifex</i>	100%
1.18%	<i>Rhodoferax antarcticus</i>	98%
1.04%	<i>Gallionella capsiferriformans</i>	97%
1.03%	<i>Sediminibacterium salmoneum</i>	99%
1.02%	<i>Thiobacillus thioparus</i>	95%

---

Table S25 - OTU sequence identity of organisms at Val Sinestra sample locations  $\geq 1\%$  abundance

Sample	Sequence Abundance	Identity	Sequence similarity
<b>150906B</b> Conradins	10.03%	<i>Sideroxydans lithotrophicus</i>	99%
	9.25%	<i>Lentimicrobium saccharophilum</i>	89%
	8.80%	<i>Nitrosomonas halophila</i>	97%
	6.47%	<i>Planktosalinus lacus</i>	95%
	5.72%	<i>Gallionella capsiferriformans</i>	97%
	5.64%	<i>Ignavibacterium album</i>	94%
	2.97%	<i>Rhodobacter sediminis</i>	99%
	2.62%	<i>Acidovorax valerianellae</i>	100%
	2.54%	<i>Lutimonas halocynthiae</i>	95%
	2.28%	<i>Polyangiaceae Byssovorax</i>	91%
	2.02%	<i>Aquimarina longa</i>	92%
	1.84%	<i>Pseudofulvimonas gallinarii</i>	95%
	1.80%	<i>Ignavibacterium album</i>	92%
	1.69%	<i>Altererythrobacter sediminis</i>	100%
	1.48%	<i>Algisphaera agarilytica</i>	85%
	1.20%	<i>Immundisolibacter cernigliae</i>	94%
	1.15%	<i>Gallionella capsiferriformans</i>	97%
	1.15%	<i>Roseovarius azorensis</i>	100%
	1.07%	<i>Acidovorax delafieldii</i>	99%
<b>150906C</b> Unnamed spring	44.93%	<i>Gallionella capsiferriformans</i>	97%
	9.39%	<i>Sulfuricurvum kujiense</i>	97%
	4.86%	<i>Acidovorax valerianellae</i>	100%
	3.56%	<i>Silanimonas mangrovi</i>	99%
	3.52%	<i>Pseudofulvimonas gallinarii</i>	95%
	2.97%	<i>Geofilum rhodophaeum</i>	92%
	2.62%	<i>Lutimonas halocynthiae</i>	95%
	2.39%	<i>Aquimarina longa</i>	92%
	1.78%	<i>Altererythrobacter sediminis</i>	100%
	1.37%	<i>Sideroxydans lithotrophicus</i>	99%
	1.04%	<i>Gallionella capsiferriformans</i>	97%
<b>150908H</b> River outlet	10.53%	<i>Sulfuricurvum kujiense</i>	97%
	9.67%	<i>Gallionella capsiferriformans</i>	97%
	4.39%	<i>Acidovorax valerianellae</i>	100%
	4.08%	<i>Desulfonatronum thiosulfatophilum</i>	90%
	4.04%	<i>Thiobacillus thioparus</i>	95%
	3.59%	<i>Melioribacter roseus</i>	91%
	3.40%	<i>Acidovorax delafieldii</i>	99%
	3.38%	<i>Geothrix fermentans</i>	96%
	2.69%	<i>Bellilinea caldifistulae</i>	90%
	2.34%	<i>Rubrobacter radiotolerans</i>	84%
	2.25%	<i>Aquimarina longa</i>	92%
	2.24%	<i>Desulfitispora elongata</i>	89%
	1.65%	<i>Silanimonas mangrovi</i>	99%
	1.49%	<i>Anaeromyxobacter dehalogenans</i>	92%
	1.46%	<i>Prolixibacter denitrificans</i>	90%
	1.39%	<i>Gallionella capsiferriformans</i>	97%
	1.35%	<i>Anaeromyxobacter dehalogenans</i>	89%



1.27%	<i>Sideroxydans lithotrophicus</i>	99%
1.20%	<i>Labilibacter aurantiacus</i>	90%
1.08%	<i>Rhodobacter sediminis</i>	99%

Table S26 - OTU sequence identity of organisms at Alvaneu sample locations  $\geq 1\%$  abundance

Sample	Sequence Abundance	Identity	Sequence similarity
<b>150905A</b> Arvadi	4.02%	<i>Thiobacillus thioparus</i>	98%
	2.60%	<i>Nitrospira japonica</i>	95%
	2.28%	<i>Sulfuricaulis limicola</i>	92%
	2.05%	<i>Acidovorax valerianellae</i>	100%
	1.57%	<i>Thiofaba tepidiphila</i>	95%
	1.49%	<i>Hyphomicrobium nitrativorans</i>	96%
	1.26%	<i>Thiohalobacter thiocyanaticus</i>	90%
	1.21%	<i>Lysinibacillus alkalisoli</i>	87%
	1.10%	<i>Chryseolinea serpens</i>	94%
	1.09%	<i>Arenimonas daejeonensis</i>	100%
<b>150911T</b> Eisenquelle	9.54%	<i>Methylovulum psychrotolerans</i>	97%
	7.23%	<i>Sideroxydans lithotrophicus</i>	99%
	6.33%	<i>Nitrospira japonica</i>	95%
	3.89%	<i>Geobacter psychrophilus</i>	97%
	2.15%	<i>Acidovorax valerianellae</i>	100%
	1.91%	<i>Propionivibrio dicarboxylicus</i>	97%
	1.55%	<i>Aureimonas pseudogalii</i>	97%
	1.40%	<i>Anaeromyxobacter dehalogenans</i>	92%
	1.28%	<i>Sideroxydans lithotrophicus</i>	98%
	1.14%	<i>Gallionella capsiferriiformans</i>	97%
	1.06%	<i>Sulfurisoma sediminicola</i>	98%

Table S27 - OTU sequence identity of organisms at Jöri lake sample locations  $\geq 1\%$  abundance

Sample	Sequence Abundance	Identity	Sequence similarity
<b>150909N</b>	9.3%	<i>Labilibacter aurantiacus</i>	90%
Jöri Lake XIII	3.9%	<i>Methylobacter tundripaludum</i>	98%
10 meter depth	3.4%	<i>Lysinibacillus alkalisoli</i>	87%
	3.4%	<i>Acidovorax valerianellae</i>	100%
	1.9%	<i>Limisphaera ngatamarikiensis</i>	90%
	1.3%	<i>Litorilinea aerophila</i>	88%
	1.2%	<i>Anaeromyxobacter dehalogenans</i>	97%
	1.1%	<i>Limisphaera ngatamarikiensis</i>	89%
<b>150909L</b>	6.86%	<i>Bradyrhizobium lupini</i>	99%
Jöri lake XIII outflow	5.74%	<i>Ilumatobacter coccineus</i>	92%
	4.72%	<i>Caldalkalibacillus uzonensis</i>	87%
	2.96%	<i>Nitrospira japonica</i>	95%
	2.53%	<i>Pseudonocardia xishanensis</i>	100%
	2.23%	<i>Acidovorax valerianellae</i>	100%
	2.00%	<i>Gemmatimonas aurantiaca</i>	92%
	1.77%	<i>Pyxidicoccus fallax</i>	91%
	1.66%	<i>Vicinamibacter silvestris</i>	92%
	1.60%	<i>Granulicella acidiphila</i>	88%
	1.23%	<i>Sulfuritortus calidifontis</i>	95%
	1.11%	<i>Elstera cyanobacteriorum</i>	93%
<b>150909M</b>	6.43%	<i>Caldalkalibacillus uzonensis</i>	87%
Jöri lake XXI	4.38%	<i>Gemmatimonas phototrophica</i>	90%
	3.86%	<i>Granulicella acidiphila</i>	88%
	2.02%	<i>Luteitalea pratensis</i>	88%
	1.64%	<i>Janthinobacterium svalbardensis</i>	96%
	1.43%	<i>Nitrospira japonica</i>	95%
	1.27%	<i>Acidovorax valerianellae</i>	100%
	1.22%	<i>Parvibaculum lavamentivorans</i>	87%
	1.19%	<i>Gemmatimonas phototrophica</i>	91%
	1.17%	<i>Vicinamibacter silvestris</i>	92%
	1.10%	<i>Nitrosospira multiformis</i>	95%
	1.04%	<i>Acidicapsa acidisoli</i>	87%
	1.03%	<i>Azospirillum humicireducens</i>	94%
	1.02%	<i>Lysinibacillus alkalisoli</i>	87%
<b>150910O</b>	4.03%	<i>Lysinibacillus alkalisoli</i>	87%
Jöri lake II	3.02%	<i>Labilibacter aurantiacus</i>	90%
	2.48%	<i>Methylobacter tundripaludum</i>	98%
	2.15%	<i>Nitrospira japonica</i>	95%
	2.04%	<i>Acidovorax valerianellae</i>	100%
	1.96%	<i>Thermomarinilinea lacunifontana</i>	89%
	1.40%	<i>Calditerricola yamamuriae</i>	100%
	1.38%	<i>Methylobacter halotolerans</i>	88%
	1.15%	<i>Methylobacterium petroleiphilum</i>	99%
	1.14%	<i>Enterococcus gallinarum</i>	87%
<b>150910R</b>	3.94%	<i>Gemmatimonas phototrophica</i>	90%
Jöri lake XVIII	2.68%	<i>Gemmatimonas phototrophica</i>	91%
	2.36%	<i>Nitrospira japonica</i>	95%

2.07%	<i>Caldalkalibacillus uzonensis</i>	87%
1.79%	<i>Flaviumibacter stibioxidans</i>	96%
1.57%	<i>Acidovorax valerianellae</i>	100%
1.52%	<i>Janthinobacterium svalbardensis</i>	96%
1.51%	<i>Geobacter psychrophilus</i>	98%
1.45%	<i>Geobacter psychrophilus</i>	97%
1.25%	<i>Chryseolinea serpens</i>	92%
1.11%	<i>Methylibium petroleiphilum</i>	99%
1.09%	<i>Geobacter argillaceus</i>	98%

---

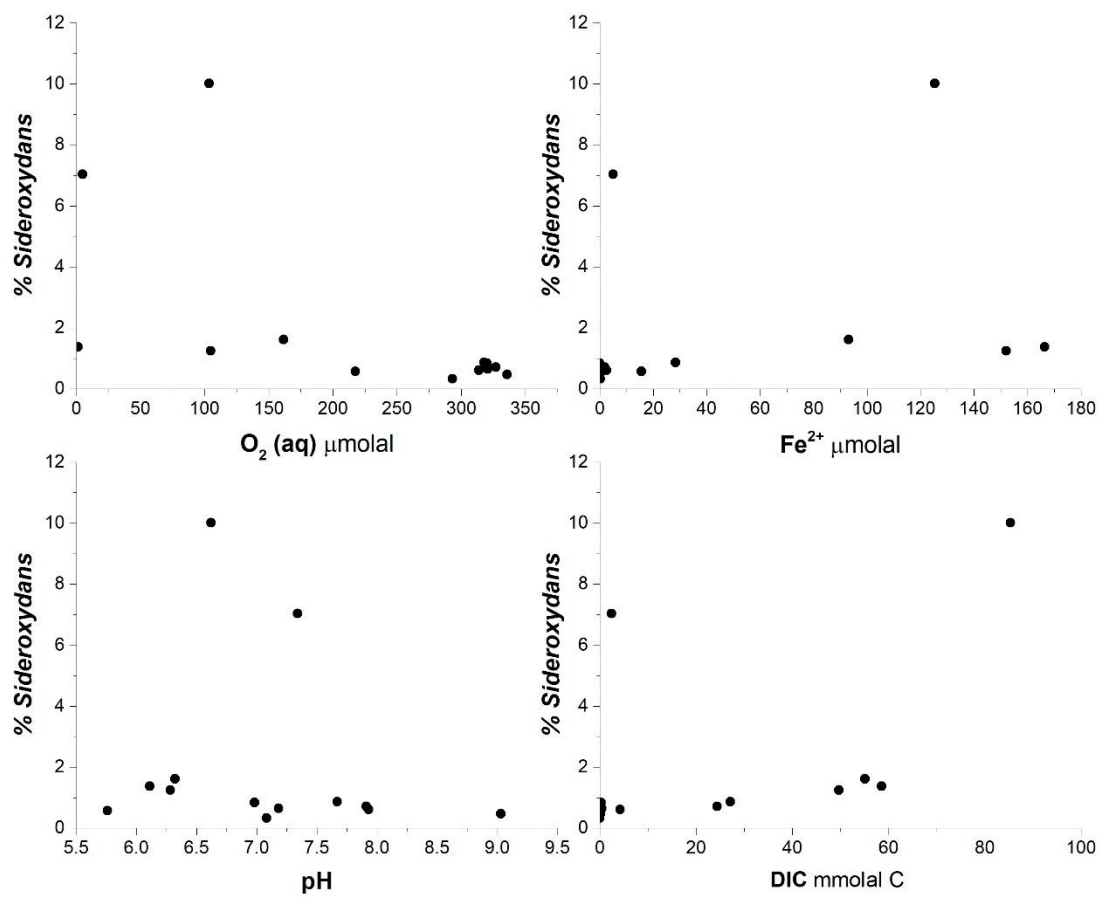


Figure S16 – Abundance of *Sideroxydans* genus OTUs (as determined by the Silva database) plotted against  $O_2$ ,  $Fe^{2+}$ , pH, and DIC concentrations. Niche specialization is not as apparent as closely related *Gallionella* OTUs (Fig 10).

## References for Supplementary Material

Reference numbering is continued from the main text.

69. Helgeson, H.; Kirkham, D.; Flowers, G. Theoretical prediction of the thermodynamic behavior of aqueous electrolytes at high pressures and temperatures: IV. Calculation of activity coefficients, osmotic coefficients, and apparent molal and standard and relative partial molal properties to 600 °C and 5 Kb. *Am. J. Sci.* **1981**, *281*, 1249-1516.
70. Canovas, P.; Shock, E. Geobiochemistry of metabolism: Standard state thermodynamic properties of the citric acid cycle. *Geochim. Cosmochim. Acta.* **2016**, *195*, 293-322.
71. Prapaipong, P.; Shock, E.; Koretsky, C. Metalorganic complexes in geochemical processes: temperature dependence of standard partial molal thermodynamic properties of aqueous complexes between metal cations and dicarboxylate ligands. *Geochim. Cosmochim. Acta.* **1999**, *63*, 2547–2577.
72. Haas, J.; Shock, E.; Sassani, D. Rare earth elements in hydrothermal systems: Estimates of standard partial molal thermodynamic properties of aqueous complexes of the rare earth elements at high pressures and temperatures. *Geochim. Cosmochim. Acta.* **1995**, *59*, 4329-4350.
73. Preis, W. and Gamsjäger, H. Critical evaluation of solubility data: enthalpy of formation of siderite. *Phys. Chem. Chem. Phys.* **2002**, *4*, 4014-4019.
74. Kubota, E.; Mochizuki, Y.; Yokoi, M. Conductivity of iron(II) sulfate in aqueous solution at various temperatures. *Bull. Chem. Soc. Jpn.* **1988**, *61*, 3723-3724.
75. Byrne, R. and Miller, W. Copper(II) carbonate complexation in seawater. *Geochim. Cosmochim. Acta* **1985**, *49*, 1837-1844.
76. Sunda, W. and Hanson, P. *Chemical Speciation of Copper in River Water* in Chemical Modeling in Aqueous Systems. *ACS Symposium Series* **1979**, *93*, 147-180.
77. Gardiner, J. The chemistry of cadmium in natural water I - A study of cadmium complex formation using the cadmium specific-ion electrode. *Water Res.* **1974**, *8*, 23-30.
78. Fouillac, C. and Criaud, A. Carbonate and bicarbonate trace-metal complexes - critical reevaluation of stability-constants. *Geochem. J.* **1984**, *18*, 297-303.
79. Bilinski, H.; Huston, R.; Stumm, W. Determination of the stability constants of some hydroxo and carbonato complexes of Pb(II), Cu(II), Cd(II) and Zn(II) in dilute solutions by anodic stripping voltammetry and differential pulse polarography. *Anal. Chim. Acta.* **1976**, *84*, 157-164.
80. Stanley, J. and Byrne, R. Inorganic complexation of Zinc (II) in seawater. *Geochim. Cosmochim. Acta* **1990**, *54*, 753-760.

81. Ryan, M. and Bauman, J. Thermodynamics of the zinc bicarbonate ion pair. *Inorg. Chem.* **1978**, *17*, 3329-3331.
82. Bilinski, H. and Schindler, P. Solubility and equilibrium constants of lead in carbonate solutions (25°C, I = 0.3 mol dm<sup>-3</sup>). *Geochim. Cosmochim. Acta.* **1982**, *46*, 921-928.
83. Néher-Neumann, E. Studies on metal carbonate equilibria. 24. The hydrogen carbonate and carbonate complexes of the lead(II) and cadmium(II) ions in acid solutions and a 3M (Na)ClO<sub>4</sub> ionic medium at 25 °C. *Acta Chem. Scand.* **1992**, *46*, 231-239.
84. Vinson, M.; Arvidson, R.; Luttge, A. Kinetic inhibition of calcite dissolution by aqueous manganese(II). *J. Cryst. Growth.* **2007**, *307*, 116-125.
85. Mattigod, S. and Sposito, G. Estimated association constants for some complexes of trace metals with inorganic ligands. *Soil Sci. Soc. Am. J.* **1977**, *41*, 1092-1097.
86. Nakayama, F. Thermodynamic functions for the dissociation of NaHCO<sub>3</sub><sup>0</sup>, NaCO<sub>3</sub><sup>-</sup>, H<sub>2</sub>CO<sub>3</sub> and HCO<sub>3</sub><sup>-</sup>. *J. Inorg. Nucl. Chem.* **1971**, *33*, 1287-1291.
87. Wimberley, P.; Siggaardandersen, O.; Foghandersen, N.; Boink, A. Are sodium-bicarbonate and potassium bicarbonate fully dissociated under physiological conditions? *Scand. J. Clin. Lab. Invest.* **1985**, *45*, 7-10.
88. Koslov, V.K. The role of carbonate complexes in hydrothermal silver transport. *Geochem. Int.* **1985**, *22*, 85-95.
89. Siebert, R. and Hostetler, P. The stability of the magnesium bicarbonate ion pair from 10 °C to 90 °C. *Amer. J. Sci.* **1977**, *277*, 697-715.
90. Plummer, L. and Busenberg, E. The solubilities of calcite, aragonite and vaterite in CO<sub>2</sub>-H<sub>2</sub>O solutions between 0 and 90 °C and an evaluation of the aqueous model for the system CaCO<sub>3</sub>-CO<sub>2</sub>-H<sub>2</sub>O. *Geochim. Cosmochim. Acta.* **1982**, *46*, 1011 – 1040.
91. Busenberg, E.; Plummer, L.; Parker, V. The solubility of strontianite (SrCO<sub>3</sub>) in CO<sub>2</sub>-H<sub>2</sub>O solutions between 2 and 91°C, the association constants of SrHCO<sup>+</sup> (aq) and SrCO<sub>3</sub> (aq) between 5 and 80°C, and an evaluation of the thermodynamic properties of Sr<sup>2+</sup> (aq) and SrCO<sub>3</sub> (cr) at 25°C and 1 atm total pressure. *Geochim. Cosmochim. Acta.* **1984**, *48*, 2021-2035.
92. Busenberg, E. and Plummer, L. The solubility of BaCO<sub>3</sub>(cr) (witherite) in CO<sub>2</sub>-H<sub>2</sub>O solutions between 0 and 90 °C, evaluation of the association constants of BaHCO<sub>3</sub><sup>+</sup> (aq) and BaCO<sub>3</sub><sup>0</sup> (aq) between 5 and 80 °C, and a preliminary evaluation of the thermodynamic properties of Ba<sup>2+</sup>(aq). *Geochim. Cosmochim. Acta.* **1986**, *50*, 2225-2234.
93. Powell, K.; Brown P.; Byrne, R.; Gajda, T.; Hefter, G.; Sjöberg, S.; Wanner, H. Chemical speciation of environmentally significant metals with inorganic ligands Part 2: The Cu<sup>2+</sup>, OH<sup>-</sup>, Cl<sup>-</sup>, CO<sub>3</sub><sup>2-</sup>, SO<sub>4</sub><sup>2-</sup>, and PO<sub>4</sub><sup>3-</sup> systems (IUPAC Technical Report). *Pure and Applied Chemistry.* **2007**, *79*, 895-950.

94. Powell, K.; Brown, P.; Byrne, R.; Gajda, T.; Hefter, G.; Leuz, A.; Sjöberg, S.; Wanner, H. Chemical speciation of environmentally significant metals with inorganic ligands. Part 4: the  $\text{Cd}^{2+}$ ,  $\text{OH}^-$ ,  $\text{Cl}^-$ ,  $\text{CO}_3^{2-}$ ,  $\text{SO}_4^{2-}$ , and  $\text{PO}_4^{3-}$  systems. *Pure and Applied Chemistry*. **2011**, 83, 1163.
95. Powell, K.; Brown, P.; Byrne, R.; Gajda, T.; Hefter, G.; Leuz, A.; Sjöberg, S.; Wanner, H. Chemical speciation of environmentally significant metals with inorganic ligands. Part 5: The  $\text{Zn}^{2+}$ ,  $\text{OH}^-$ ,  $\text{Cl}^-$ ,  $\text{CO}_3^{2-}$ ,  $\text{SO}_4^{2-}$ , and  $\text{PO}_4^{3-}$  systems (IUPAC Technical Report). *Pure and Applied Chemistry*. **2013**, 85, 2249-2311.
96. Powell, K.; Brown, P.; Byrne, R.; Gajda, T.; Hefter, G.; Leuz, A.; Sjöberg, S.; Wanner, H. Chemical speciation of environmentally significant metals with inorganic ligands. Part 3: The  $\text{Pb}^{2+}$ ,  $\text{OH}^-$ ,  $\text{Cl}^-$ ,  $\text{CO}_3^{2-}$ ,  $\text{SO}_4^{2-}$ , and  $\text{PO}_4^{3-}$  systems (IUPAC Technical Report). *Pure and Applied Chemistry*. **2009**, 81, 2425-2476.
97. Smith, R.; Martell, A. Inorganic Ligands. In *Critical Stability Constants: Inorganic Complexes*; Smith, R. M., Martell, A. E., Eds.; Springer US: Boston, MA, **1976**; pp 1-129.
98. Mori, J.; Neu, T.; Lu, S.; Händel, M.; Totsche, K.; Küsel, K. Iron encrustations on filamentous algae colonized by *Gallionella*-related bacteria in a metal-polluted freshwater stream. *Biogeosci.* **2015**, 12, 5277-5289.
99. Kreis, H. Die Jöriseen und ihre postglaziale Besiedlungsgeschichte. Eine faunistisch-biologische Studie. *Int Rev. ges. Hydrobiol. Hydrogeog.* **1921**, 9, 189-212.
100. Hinder, B.; Gabathuler, M.; Steiner, B.; Hanselmann, K.; Preisig, H. Seasonal dynamics and phytoplankton diversity in high mountain lakes (Jöri lakes, Swiss Alps). *J. Limnol.* **1999a**, 58, 152-161.
101. Hinder, B.; Baur, I.; Hanselmann, K.; Schanz, F. Microbial food web in an oligotrophic high mountain lake (Jöri Lake III, Switzerland). *J. Limnol.* **1999b**, 58, 162-168.